

Supplementary Information for

Ligand-bridged charge extraction and enhanced quantum efficiency enable efficient n-i-p perovskite/silicon tandem solar cells

Erkan Aydin^{1*}, Jiang Liu¹, Esma Ugur¹, Randi Azmi¹, George T. Harrison¹, Yi Hou², Bin Chen², Shynggys Zhumagali¹, Michele De Bastiani¹, Mingcong Wang¹, Waseem Raja¹, Thomas G. Allen¹, Atteq ur Rehman¹, Anand Selvin Subbiah¹, Maxime Babics¹, Aslihan Babayigit^{1,4}, Furkan H. Isikgor¹, Kai Wang¹, Emmanuel Van Kerschaver¹, Leonidas Tsetseris³, Edward H. Sargent², Frédéric Laquai¹, Stefaan De Wolf^{1*}

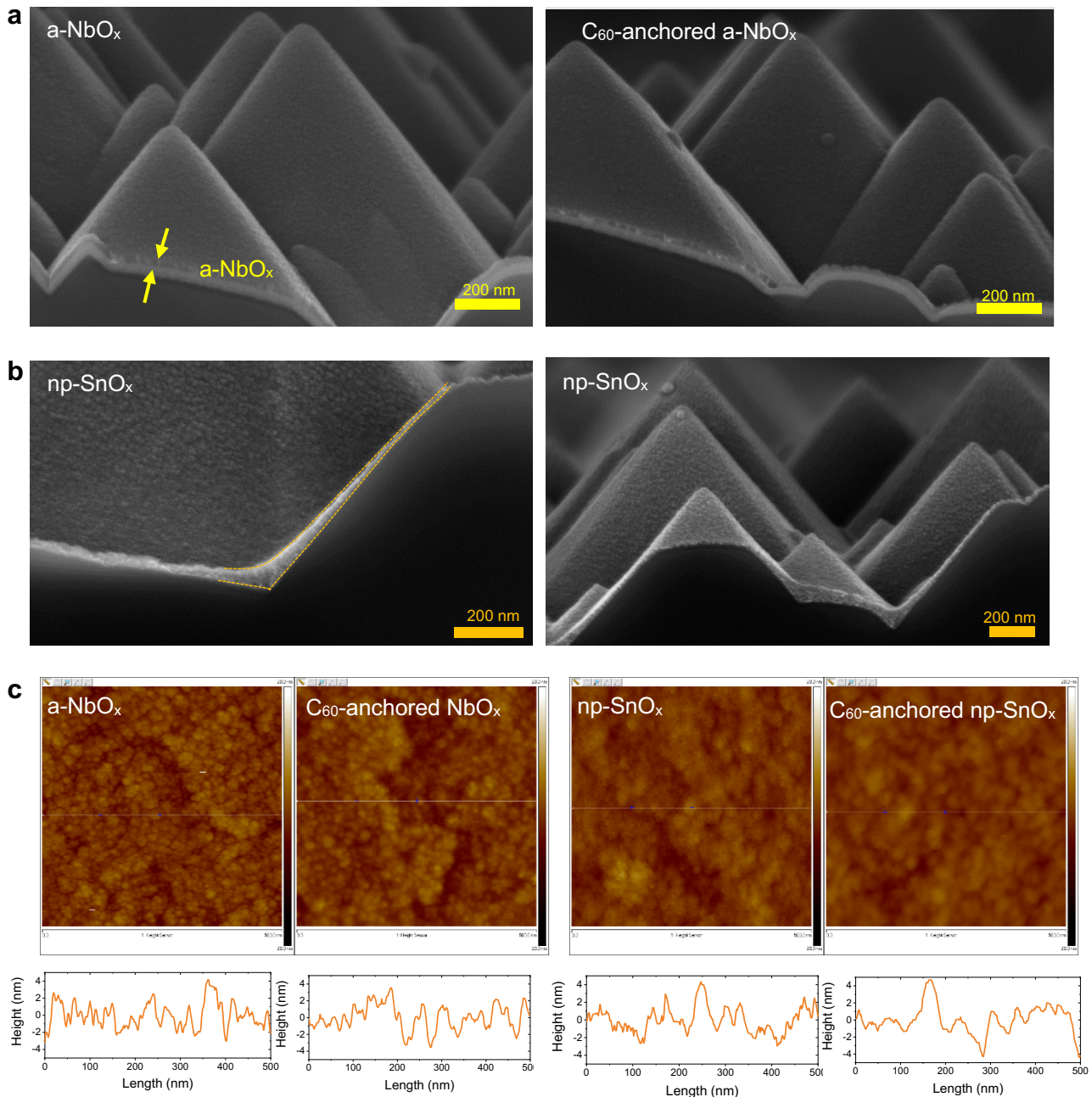
Correspondence to: erkan.aydin@kaust.edu.sa; stefaan.dewolf@kaust.edu.sa

¹King Abdullah University of Science and Technology (KAUST), KAUST Solar Center (KSC), Physical Sciences and Engineering Division (PSE), Thuwal 23955-6900, Kingdom of Saudi Arabia

²University of Toronto, Department of Electrical and Computer Engineering, Toronto, Ontario M5S 1A4, Canada

³National Technical University of Athens, Department of Physics, GR15780 Athens, Greece

⁴Hasselt University, Institute for Materials Research (IMO), Wetenschapspark 1, 3590 Diepenbeek, Limburg, Belgium.



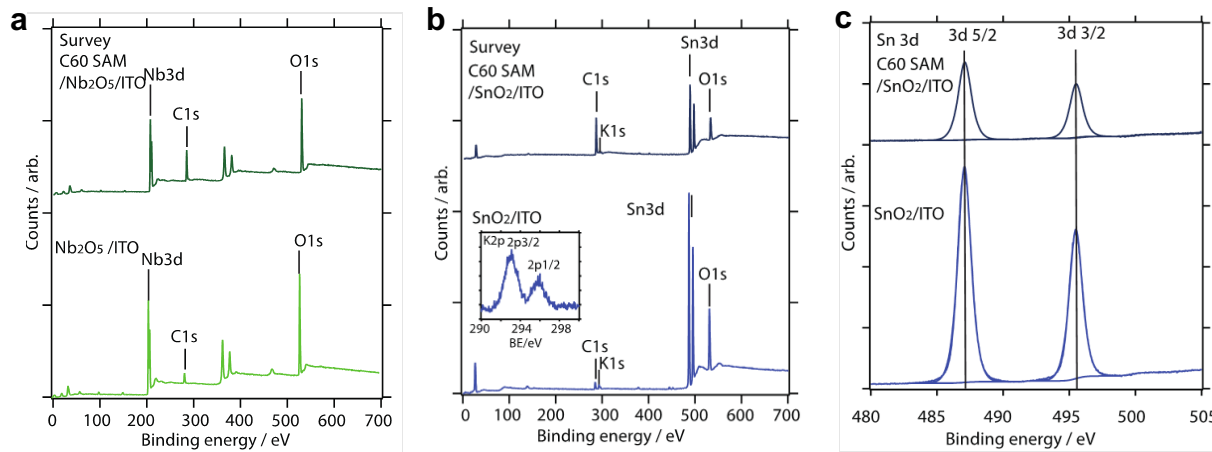
Supplementary Fig. 1. Surface morphology of a-NbO_x with and without C₆₀-anchoring. **a**, SEM cross-section images of the SHJ bottom cell with 20 nm a-NbO_x samples without any surface modification and with C₆₀-anchoring, and **b**, with spin-casted np-SnO_x. a-NbO_x films on the micron-sized pyramidal textured silicon bottom cells are conformal without any notable thickness changes across the different parts of the pyramids. However, np-SnO_x shows huge thickness variations across the profile. **c**, AFM surface morphology of the a-NbO_x films without and with C₆₀-anchoring. The average surface roughness of the neat a-NbO_x is 1.39 nm, while the C₆₀-anchored one is 1.49 nm. For np-SnO_x films, the non-modified one is 1.27 nm, and the C₆₀-anchored one is 1.05 average roughness for the scanned lines. All these average roughness values are in the same range and do not change after C₆₀-anchoring significantly.

Supplementary Note- 1: XPS analysis of the neat and C₆₀-anchored a-NbO_x and np-SnO_x films

High-resolution XPS spectra of the a-NbO_x and np-SnO_x films reveal that Nb and Sn ions exist in single metal oxide environments of Nb⁵⁺ and Sn⁴⁺ with Nb 3d 5/2 (207.3 eV) and Sn 3d 5/2 (487.07 eV) simple 3d doublets attributed to a-NbO_x, and np-SnO_x, respectively as opposed to a mixture of oxidation states. The binding energy (BE) and doublet splitting of Nb⁵⁺ fit well with that of previously reported sputtered films (207.3 - 207.2 eV).¹ The Sn 3d 5/2 BE compares with low temperature prepared np-SnO_x films.² The O 1s peak, which is located at a BE of 531 eV, display a majority of metal oxide, as shown in **Supplementary Fig. 2**, with a minor shoulder at 32.4 eV attributed to hydroxyl or oxyhydroxyl feature OH (M-OH/OH₂).^{3,4} After the C₆₀-SAM anchoring, the BEs of the Nb⁵⁺ and Sn⁴⁺ are invariant (both referenced to initial a-carbon), suggesting no Fermi level shift occurs on the top metal oxide surface of the film in contact with C₆₀-SAM.⁵

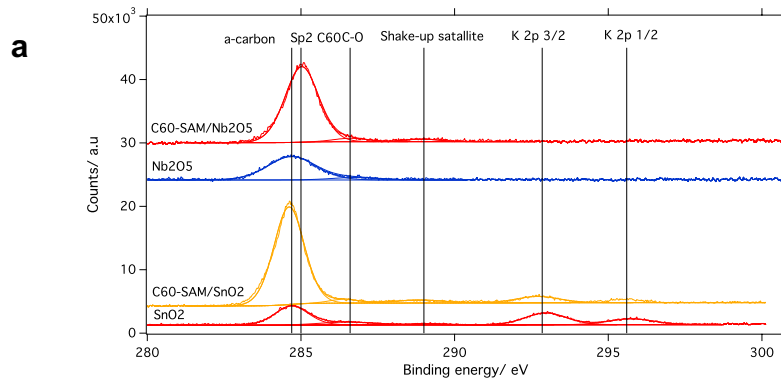
Elemental quantification of the surfaces of a-NbO_x and np-SnO_x films

From XPS analysis, we found that whereas a-NbO_x has an atomic percentage ratio of Nb/O = 1/2.52, np-SnO_x has Sn/O = 1/2.09, which are showing the nearly stoichiometric character of the films. Considering the minor hydroxyl/oxyhydroxyl peak, centered around 532.4 eV, which is 11% and 22% for a-NbO_x and SnO_x, these values are re-evaluated as Nb/O_{MetalOxide} = 1/2.2 and Sn/O_{MetalOxide} = 1/1.8 indicating these metal oxide films to be slightly sub-stoichiometric. Here, the majority of the water/OH/O_{ads} result from environmental contamination or solution film formation; however, a small fraction will result from surface bridging M-OH-M and M-OH species and resulting in a slight overestimate the percentage of water/OH/O_{ads}. XPS survey spectra revealed that solution process np-SnO_x layers show the presence of K (~3.3%) impurities, magnified peak shown in inset **Supplementary Fig. 2b**, which was reported previously.⁶



Supplementary Fig. 2. XPS survey spectra of the ESLs. Survey spectra of pristine and C₆₀-SAM anchored **a**, a-NbO_x, and **b**, np-SnO_x thin films in the survey spectra of the main elemental peaks. **c**, HR spectra of Sn 3d before and after C₆₀-SAM anchoring.

The elemental quantification of the films was determined by peak area integration of the specific peak from a wide survey scan. The individual raw peak areas are normalized for the orbital sensitivity (Scofield relative sensitivity factors (RSF)), instrumental transmission function, and the electron inelastic mean free path (IMFP) to obtain comparative elemental percentages within the CASA XPS analysis software. This region of analysis is estimated to be the first 5-10 nm depth. The quantification procedure was verified, producing equal elemental percentages for several core peaks in Ag test sample. XPS analysis revealed that upon C₆₀- anchoring, the metal oxide core lines are strongly attenuated with a concomitant increase in the peak at ~284.7-285 eV, corresponding to C₆₀ sp² carbon (**Supplementary Fig. 3**). This peak intensity change can give useful information about the coverage of the C₆₀-SAM molecule on np-SnO_x and a-NbO_x films. In addition, the features at 289 eV assigned to C₆₀ shake-up satellite can also be used to measure differences in chemical affinity.⁷ In order to make a qualitative comparison between the C1s region of the C₆₀-SAM modified np-SnO_x and a-NbO_x films, these peaks have been normalized to the adventitious environmental carbon. Here, we found that np-SnO_x has a relatively higher intensity. Besides, the measured 21.22 eV UPS frontier orbital region displays clearly defined and stronger C₆₀ features for the np-SnO_x film. Overall, the above-mentioned results evidence that both np-SnO_x and a-NbO_x show good affinity to the pyrrolidine group on C₆₀-molecule with pyrrolidine group.

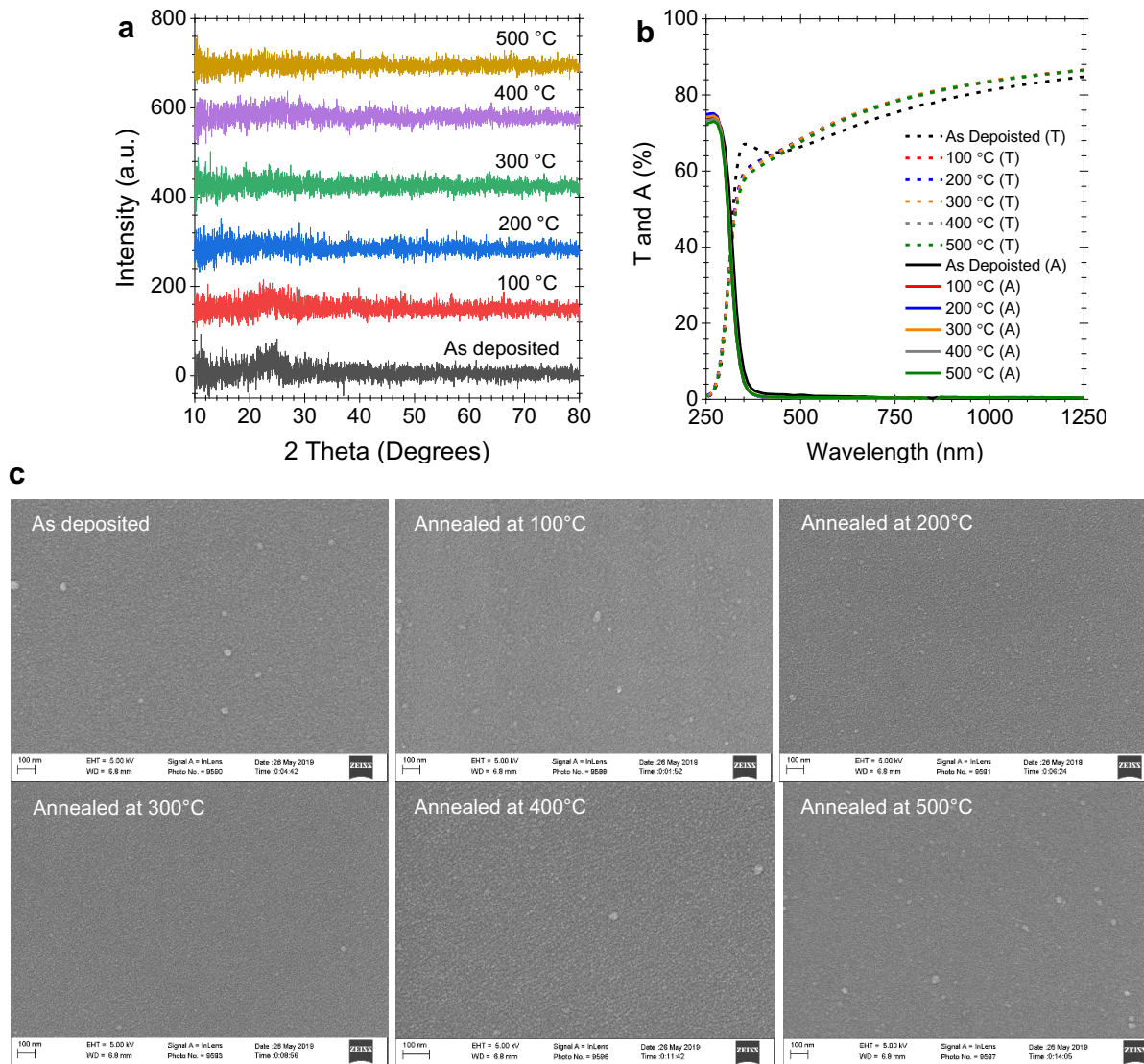


b

Samples	a-carbon	C ₆₀ carbon	Ratio C ₆₀ /a-C	C ₆₀ shake-up satellite	Ratio S/a-C
a-NbO_x	7336	N/A			
a-NbO_x / C₆₀	N/A	16501	2.224	1088.4	0.14
np-SnO_x	4137.2	N/A			
np-SnO_x / C₆₀	N/A	19453.3	4.70	935.9	0.22

Supplementary Fig. 3. C1s XPS spectra of metal oxide a-NbO_x and np-SnO_x films on ITO. Offset in the intensity for clarity recorded under identical measurement conditions. **a**, The binding energy has been calibrated to the a-carbon present on the pristine films at 284.7 eV. Vertical lines indicate the positions of a-carbon, Sp₂ C₆₀, the C₆₀ shake-up satellite, and K 2p peaks. **b**, Area integrations of peaks fitted in C1s carbon envelope for np-SnO_x, C₆₀-SAM anchored np-SnO_x, a-NbO_x, and C₆₀-SAM anchored a-NbO_x.

Supplementary Note- 2: Influence of the post-annealing on the properties of a-NbO_x films



Supplementary Fig. 4. Structural analysis of annealed a-NbO_x layers. **a**, XRD graph, **b**, transmittance, and absorptance spectra, and **c**, SEM top-view images of the a-NbO_x thin films on glass substrates for as-deposited and annealed samples at different temperatures. Here, the annealing process has been performed in ambient air for 30 min, and measurements were done without C₆₀-SAM. Here, the temperature is limited by 500 °C since for the single junction devices fabrication, the best temperature resilient TCO of FTO can withstand up to this temperature.

The electrical conductivity of our as-deposited a-NbO_x films is 1.25×10^{-7} S/cm, which is very close to the reported value for fully stoichiometric films.⁸ Nevertheless, compared to np-SnO_x and TiO₂, a-NbO_x has two orders of magnitude lower conductivity (**Supplementary Table 1**). In general, increasing the oxygen flow during processing or post-annealing in an oxygen environment resulted in O-rich films either in amorphous or crystalline structures.⁹ Here, we speculate that the

post-annealing of our a-NbO_x films in an ambient atmosphere results in filling the O vacancies and decreased conductivity, as can be seen in **Supplementary Table 1**. Indeed, previous reports revealed that a small *increase* of Nb/O ratio increases the conductivity of the films drastically.^{8, 10} In line with this, the electrical conductivity of the films also decreases two orders of magnitude after the post-annealing process due to the further oxidation of the films.

Supplementary Table 1. Hall-effect measurement results of the as-deposited and annealed a-NbO_x samples together with np-SnO_x. Here, we also compare the TiO₂ samples reported in the literature.

Sample	Sheet Resistivity [Ω sq ⁻¹]	Resistivity [Ω cm]	Carrier Density [cm ⁻³]	Reference
As Deposited a-NbO _x	$3.6 \cdot 10^9$	$8.0 \cdot 10^6$	$1.3 \cdot 10^9$	
Annealed a-NbO _x at 100 °C	$1.1 \cdot 10^{13}$	$9.3 \cdot 10^7$	$1.8 \cdot 10^8$	
Annealed a-NbO _x at 200 °C	$9.3 \cdot 10^{12}$	$1.1 \cdot 10^7$	$1.6 \cdot 10^7$	
Annealed a-NbO _x at 300 °C	$2.7 \cdot 10^{11}$	$5.4 \cdot 10^8$	$3.1 \cdot 10^7$	This work
Annealed a-NbO _x at 400 °C	$3.3 \cdot 10^{10}$	$4.1 \cdot 10^8$	$4.9 \cdot 10^7$	
Annealed a-NbO _x at 500 °C	$7.5 \cdot 10^{12}$	$1.3 \cdot 10^7$	$7.5 \cdot 10^7$	
np-SnO _x (Annealed at 150 °C)	$8.1 \cdot 10^8$	$2.4 \cdot 10^3$	$9.3 \cdot 10^{15}$	This work
TiO ₂ (Annealed at 500 °C)	-	$1.0 \cdot 10^5$	$2.6 \cdot 10^{14}$	¹¹

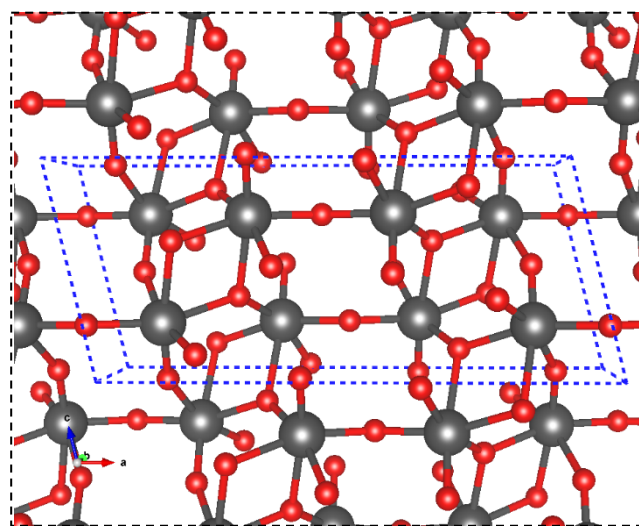
Supplementary Note- 3: DFT calculations for NbO_x and SnO_x ESLs

Calculation details

To elucidate key features related to the role of functionalized a-NbO_x as ESL, we selected one of the several possible Nb₂O₅ polymorphs to serve as an approximation for the modeling of the bulk of the material and its surface Nb₂O₅. Based on our results, crystalline phases of Nb₂O₅ are ranked as follows according to their relative stability and starting with the most stable (the number refers to space groups): #12, #3, #139, #15, #19, #11, #5. Of these structures, we selected the monoclinic phase with space group #15 (symbol C2/c, four chemical formulae in its unit cell) as the only suitable choice for our DFT modeling of bulk supercells and surface slabs (supercells of other crystal phases are too large for the calculations needed in this study).

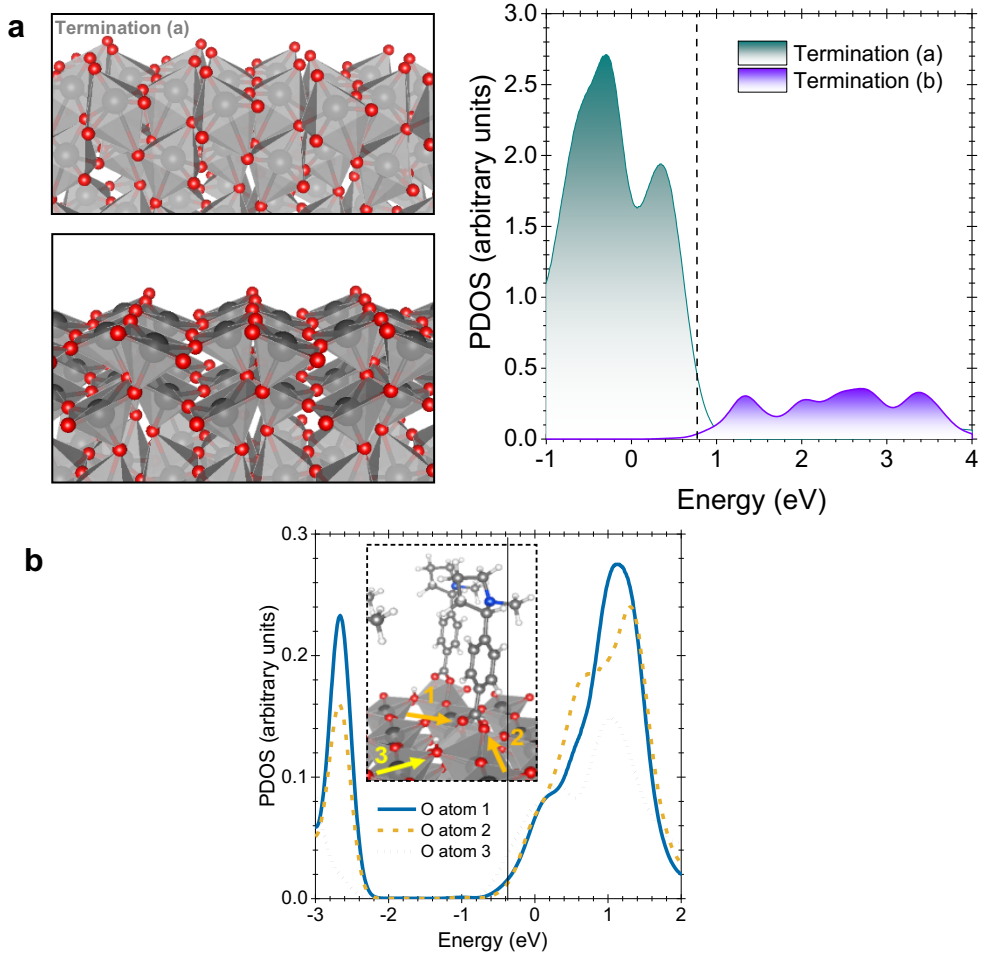
Supplementary Table 2. Relative stability and lattice parameters of Nb₂O₅ crystalline polymorphs based on DFT calculations. Z is the number of chemical formulae in the unit cell, ΔE is the energy difference (in meV) per chemical formula referenced with respect to the most stable structure.

Space Group	Z	ΔE (meV)	a (Å)	b (Å)	c (Å)	α	β	γ
#3	14	3	19.613	3.842	20.634	90.0°	115.7°	90.0°
#5	2	517	8.978	6.727	5.843	90.0°	133.3°	90.0°
#11	2	463	6.742	3.837	7.723	90.0°	89.8°	90.0°
#12	16	0	28.955	3.825	17.849	90.0°	125.1°	90.0°
#15	4	142	12.889	4.943	5.634	90.0°	103.7°	90.0°
#19	4	410	5.33	9.832	9.78	90.0°	90.0°	90.0°
#139	16	68	20.602	20.602	3.826	90.0°	90.0°	90.0°

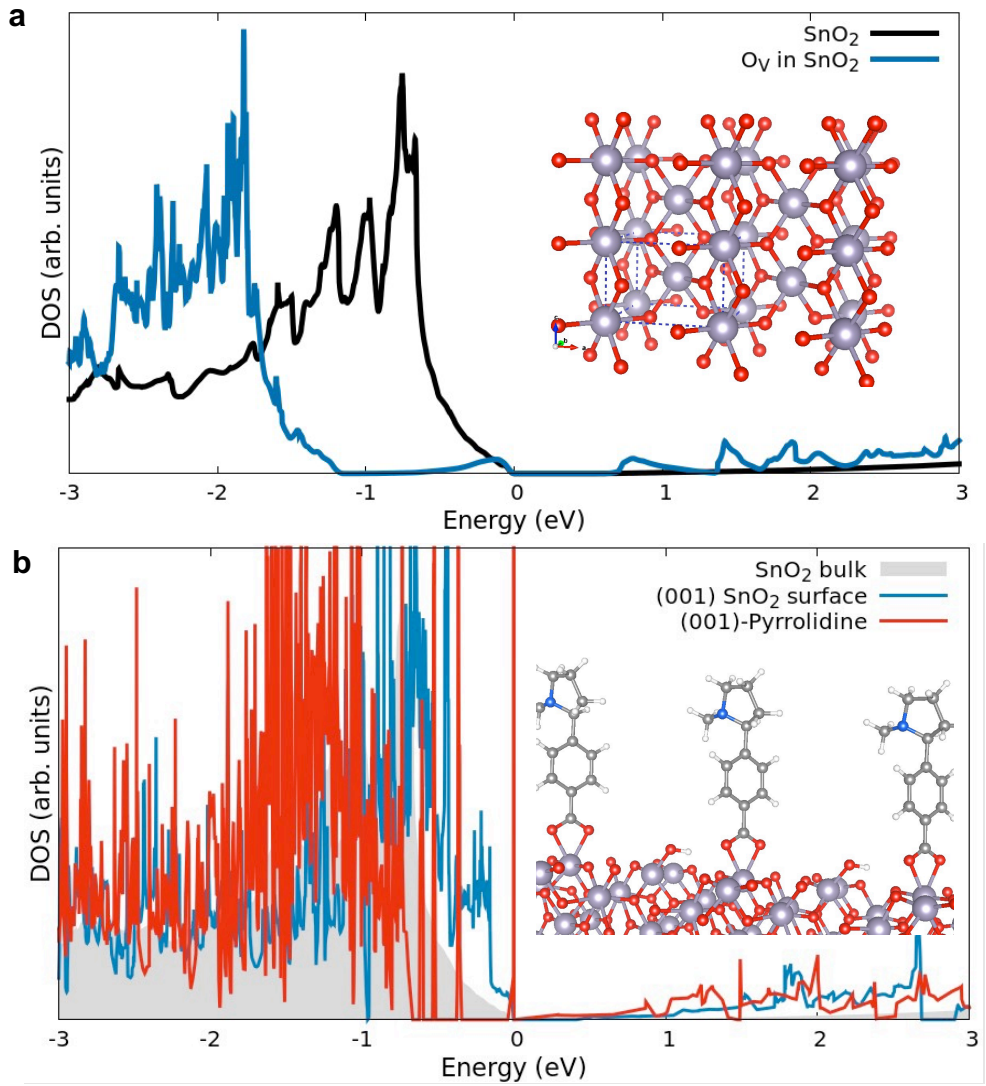


Supplementary Fig. 5. Structure of the C2/c polymorph of NbO_x. The dashed line shows the unit cell.

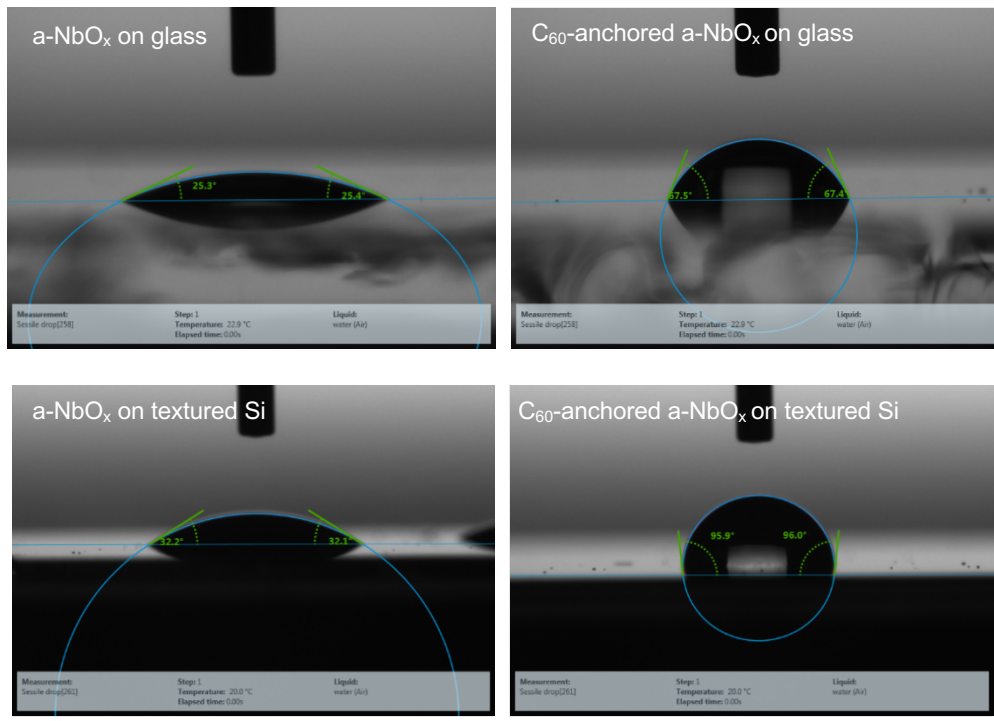
NbO_x (100) surface: structure and DOS



Supplementary Fig. 6. DOS calculations for Nb₂O₅. **a**, Projected density of states (PDOS) for an O atom on a (100) surface of NbO_x, which is terminated by (a) truncated octahedra that are missing one O atom, (b) by full octahedra (Nb: light green, O: red spheres). The dashed line shown the position of the Fermi level. A C₆₀-pyrrolidine molecule chemisorbs strongly through its pyrrolidine group on the surface shown in (b) with a binding energy of 1.63 eV. **b**, Projected density of states (PDOS) for three of the surface O atoms of the structure shown in the inset figure, which depicts the chemisorption of Pyrrolidine groups on an O-deficient NbO_x surface. The vertical line at the center shows the energy of the highest occupied states, which here lie at the bottom of the conduction band.



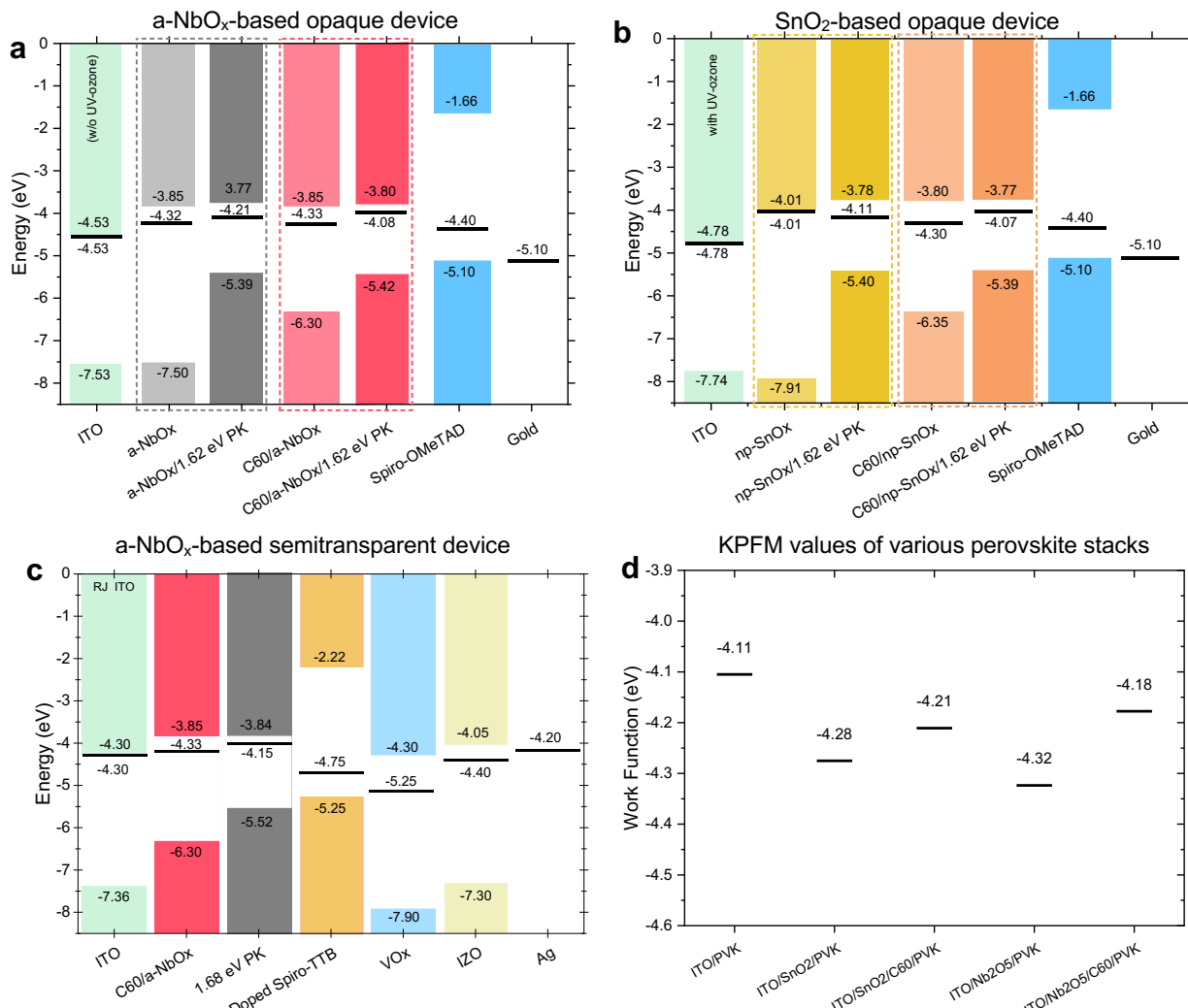
Supplementary Fig. 7. DOS calculations for SnO_x. **a**, Electronic DOS for bulk SnO₂ (black line) and a 72-atom supercell of SnO₂ with one O vacancy, O_V, (blue line). The energy of the highest occupied state in each case is set to zero. The inset shows the crystal structure of SnO₂ with its unit cell delineated by a dashed blue line (Sn: gray, O: red spheres). The O vacancy creates a state within the energy band gap of SnO₂. **b**, Electronic DOS for SnO₂ (gray background), a SnO₂-(001) surface (blue line), and a SnO₂-(001) surface with pyrrolidine molecules anchored as shown in the inset (Sn: big gray, O: red, C: gray, N: blue, H: white spheres). The energy of the highest occupied state in each case is set to zero. The pyrrolidine molecule is anchored (the adsorption energy is equal to 2.18 eV) to a surface Sn atom through its end O-atoms, and the corresponding H atom is attached to a neighboring surface O atom. As shown in the DOS plots, functionalization with pyrrolidine molecules creates a number of states within the energy band gap of SnO₂.



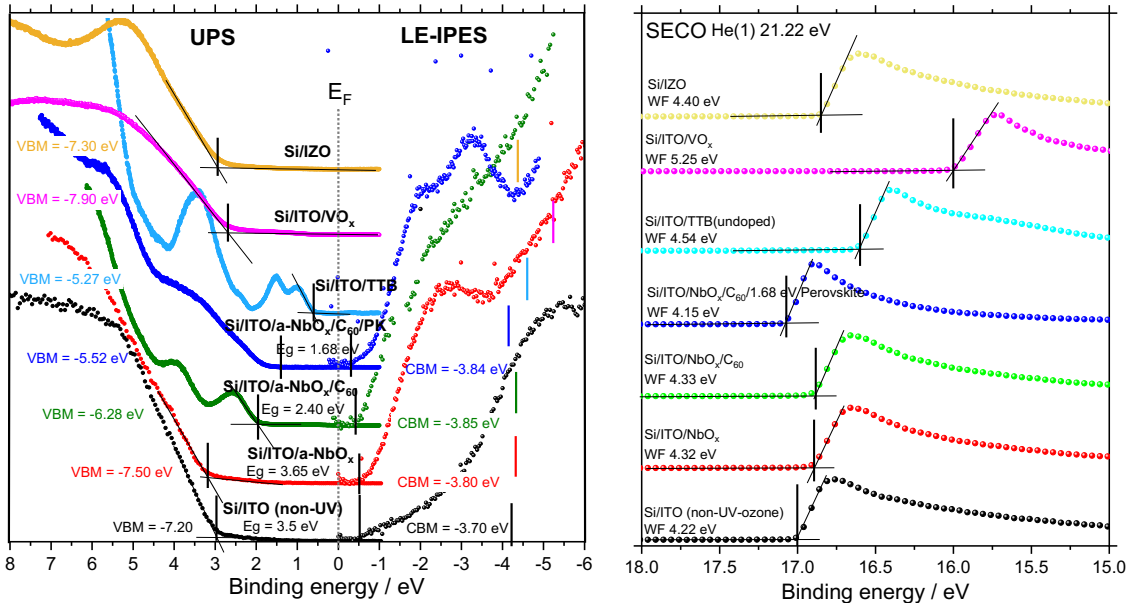
Supplementary Fig. 8. Contact angle measurements. Contact angle measurements for neat and C₆₀-anchored a-NbO_x thin films on glass substrates and textured devices. The increased contact angle proves the existence of the C₆₀-SAM layers on both flat substrates and fully-textured SHJ bottom cells.

Supplementary Note- 4: UPS and IPES analysis of the layers

Here, the UPS measurements of the perovskite layers were done on ITO/a-NbO_x/C₆₀ films. The high dependency of the E_F on the layers underneath of the perovskite might be the reason for the *n*-type character of the perovskite surface.¹²



Supplementary Fig. 9. Energy levels of layers for the opaque and semitransparent perovskite cells. Relative band edges for the layers in the opaque single-junction **a,b**, perovskite and **c**, semitransparent perovskite top cells (for perovskite/silicon tandems). The “solid black” lines represent the measured WF values of the given films. **d**, KPFM measurement results of the various stacks. Note that, for KPFM measurements, the samples were exposed to ambient air while UPS/IPES samples transferred in a vacuum.



Supplementary Fig. 10. UPS and IPES spectra of the films with a detailed view of cut-off values. V_{BM} values have been calculated using the equation of $V_{BM} = WF + E_{onset}$, E_{onset} represents the UPS photoemission onset energy.

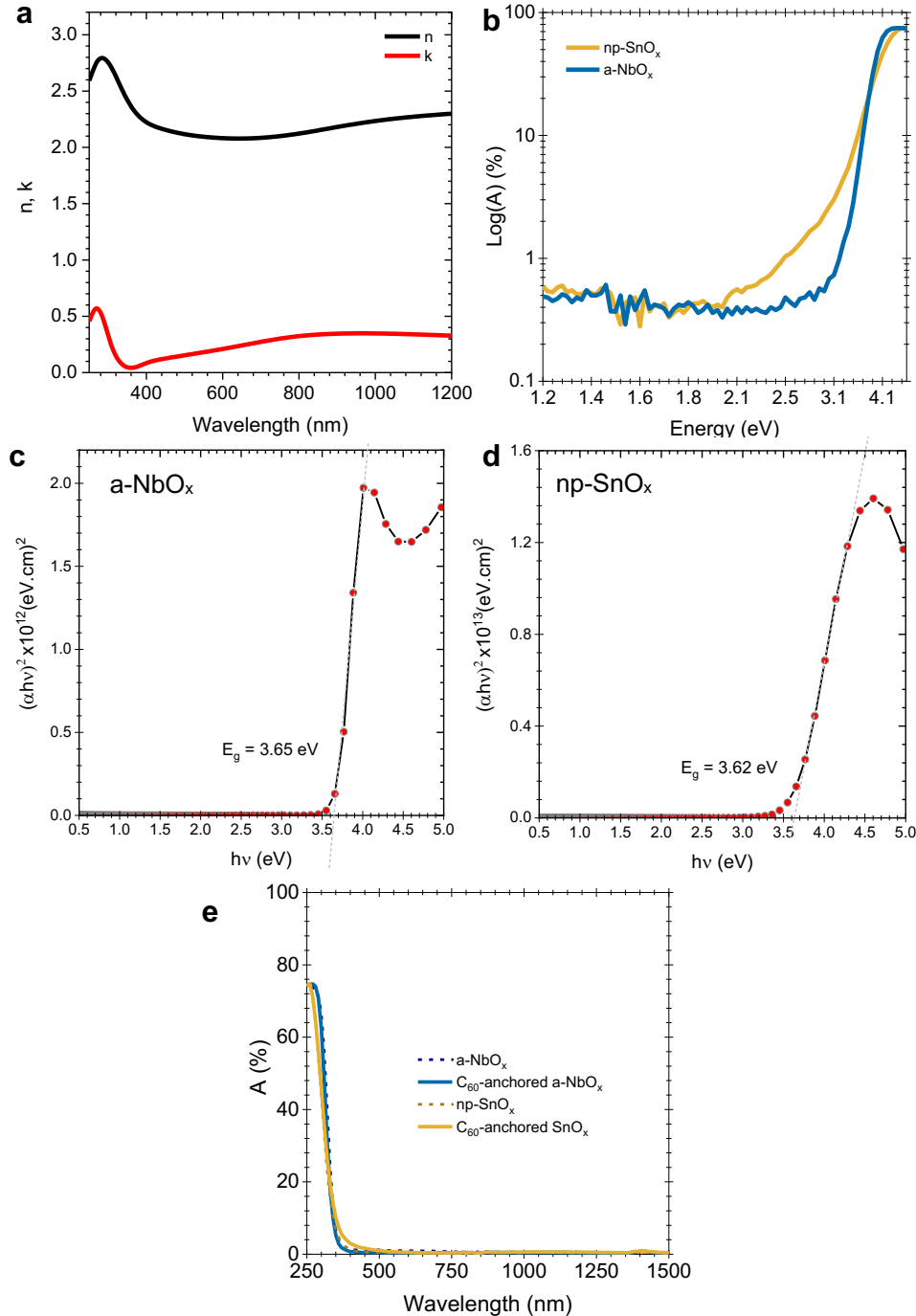
Supplementary Table 3. The direct comparison of the band edges, work function, and bandgap of the Nb_2O_5 and np- SnO_x films used in this study with other reports in the literature with different techniques.

Nb_2O_5

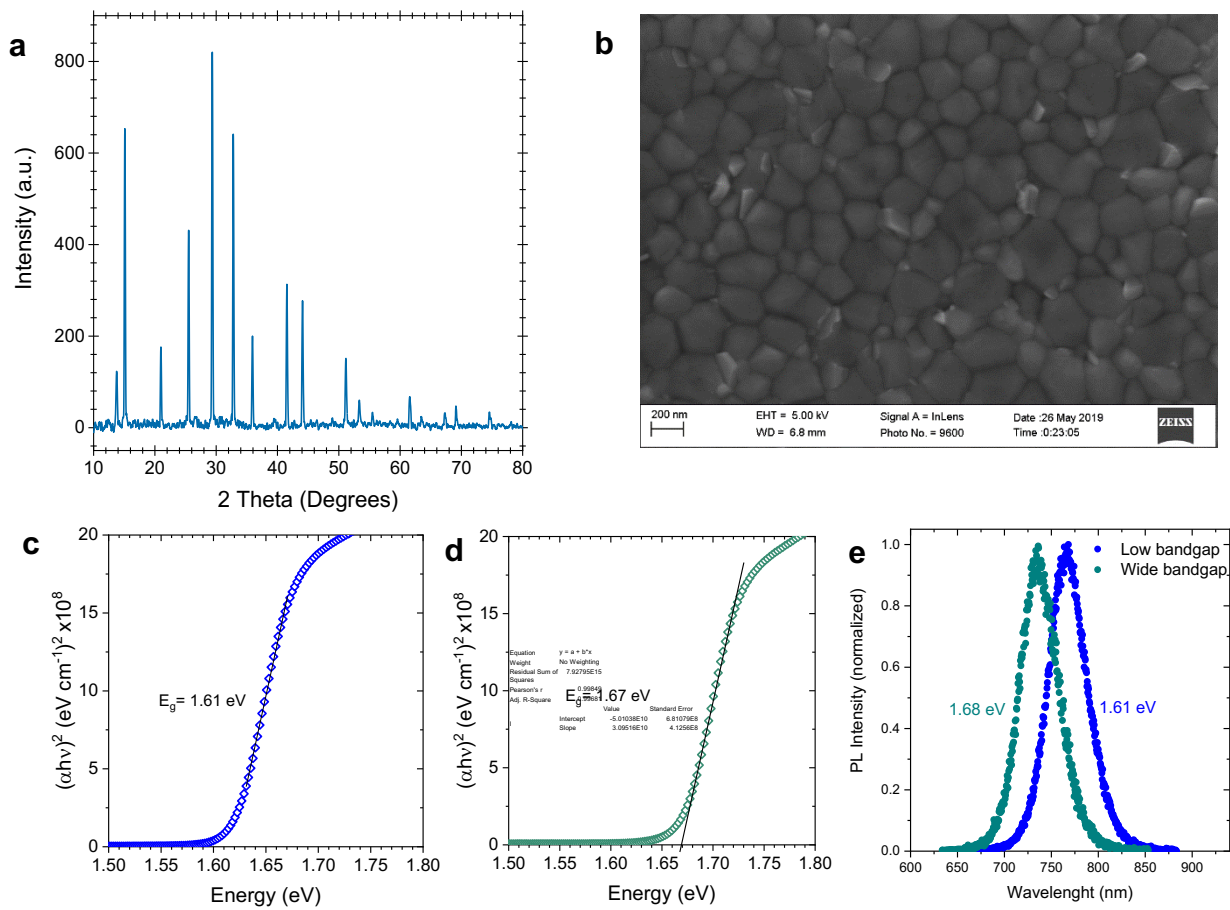
Technique	E_g (eV)	Technique	CBM (eV)	WF (eV)	V_{BM} (eV)	Ref.
Sputtering	3.85	UPS	-4.35	-4.70	-8.20	¹³
Sputtering	-	KPFM	-	-4.31	-	¹⁴
Sol-gel	3.37	UPS	-4.37	-	-7.74	¹⁵
Nanoparticle/Spin coating	3.46	UPS/KPFM	-4.33	-4.80	-7.79	¹⁶
E-beam		UPS	-	-4.25	-	¹⁷
Solution	3.41	UPS	-4.02	-6.66	-7.43	¹⁸
Solution	-	KPFM	-	-4.28	-	¹⁹
Sputtering	3.65	UPS	-3.85	-4.32	-7.50	This work
Sputtering+C₆₀	-	UPS	-3.85	-4.33	-6.30	This work

SnO_2

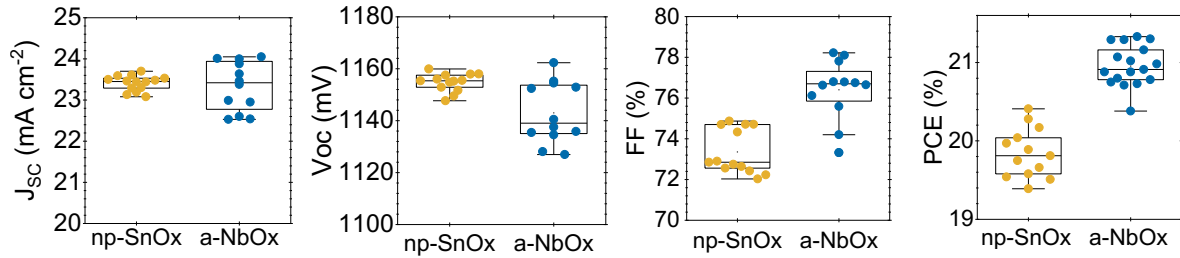
Technique	E_g (eV)	Technique	CBM (eV)	WF (eV)	V_{BM} (eV)	Ref.
Sputtering	3.72	UPS	-4.36	-5.01	-8.08	²⁰
Sputtering	3.99	UPS	-3.65	-4.20	-7.44	²¹
Solution	-	UPS	-	-4.20	-7.80	²²
Solution	3.91	UPS	-4.85	-5.16	-8.76	²³
ALD	3.25	UPS	-4.32	-4.20	-7.57	²⁴
Alfa-np	3.79	UPS	-4.31	-4.36	-8.10	²⁵
Alfa-np	3.62	UPS	-4.01	-4.01	-7.91	This work
Alfa-np+C₆₀	-	UPS	-3.80	-4.30	-6.35	This work



Supplementary Fig. 11. Optical properties of the sputtered a-NbO_x and np-SnO_x films. **a**, Spectroscopic ellipsometry data for the sputtered a-NbO_x films. **b**, Absorptance spectra of np-SnO_x and RF-sputtered a-NbO_x films in the logarithmic scale. The measured optical band gap values of the **c**, a-NbO_x, and **d**, np-SnO_x films from $(\alpha h v)^2$ vs $h v$ graphs. Here, 50 nm of a-NbO_x and 20 nm of np-SnO_x films have been deposited on bare glass substrates, and transmittance (T), reflectance (R) measurements were performed with integrating sphere. Interestingly, although our NbO_x films are amorphous, they show a steeper absorption edge, which suggests a less disordered microstructure compared to np-SnO_x films (**Supplementary Fig. 5b**). **e**, Absorptance (A) spectra of the a-NbO_x and np-SnO_x films with and without C₆₀-anchoring.



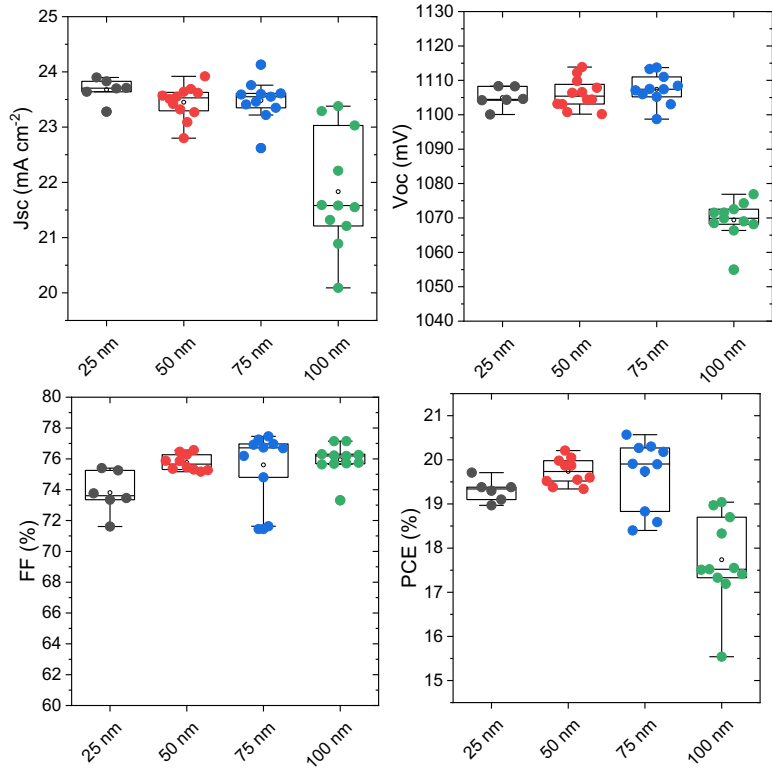
Supplementary Fig. 12. Structural and optical properties of the 1.61 eV perovskite absorber. **a**, XRD graph **b**, SEM top-view image of the perovskite absorber layer, which is used for the fabrication of the single junction devices. Excess PbI_2 phases can be seen (bright regions) at the grain boundaries. The calculated optical band gap values for **c**, low and **d**, wide bandgap perovskite for the 640 nm layer. **e**, The PL emission of the perovskite samples with different bandgaps extracted from the streak camera image. The PL peaked at ~ 738 nm corresponding to 1.68 eV (slightly different from the Tauc plot) while ~ 768 nm corresponding to 1.61 eV bandgap perovskite.



Supplementary Fig. 13. Single junction device statistics of C₆₀-anchored np-SnO_x and a-NbO_x films. Results for 1.61 eV based perovskite absorbers. Note that all devices here utilize C₆₀-anchored ESLs.

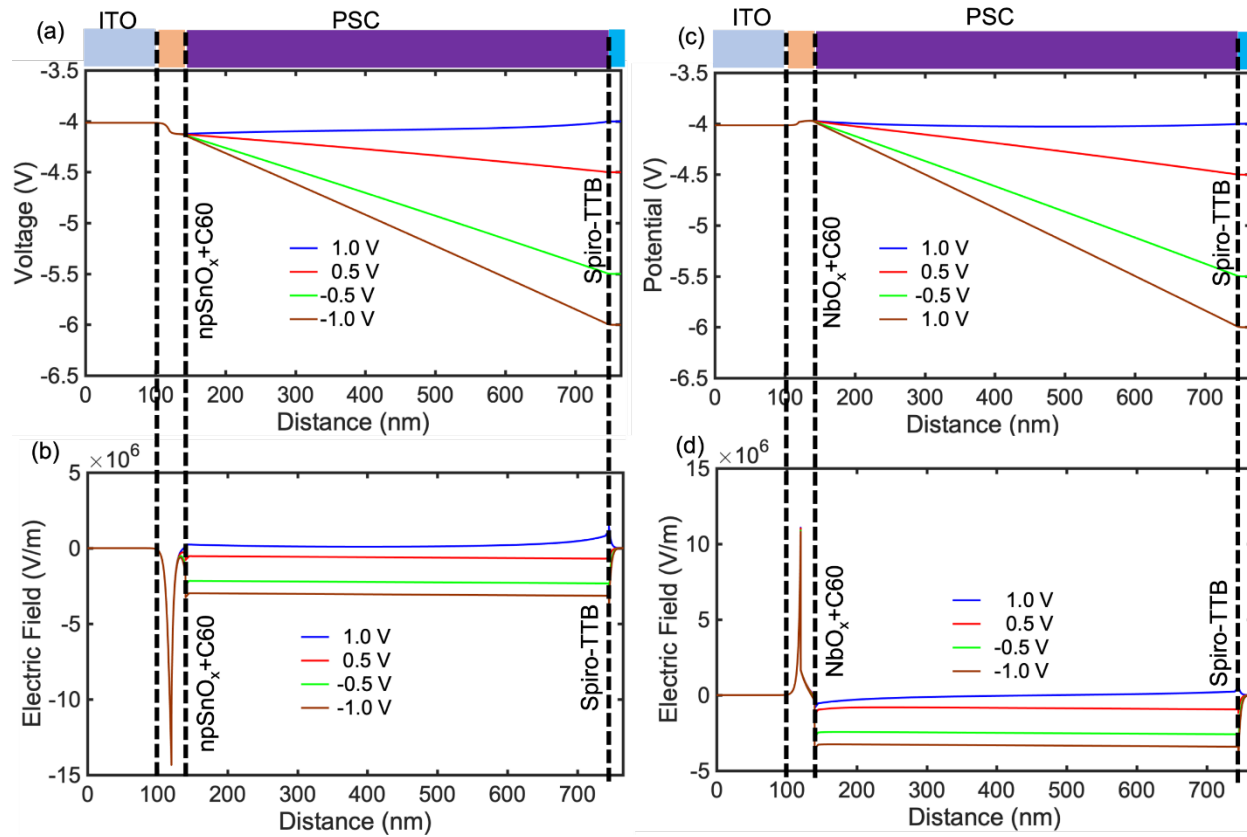
Supplementary Table 4. Performance overview for the fabricated single-junction PSCs and mini-modules. Note that, the reported devices are with 2D/3D passivation on perovskite layers and utilize doped spiro-TTB/TPBI/VO_x as HSL.

ESL stack	Perovskite Bandgap	Area	Scan Direction	Voc (mV)	J _{SC} (mA cm ⁻²)	FF (%)	PCE (%)
np-SnO _x	1. 61 eV	0.1 cm ²	Voc to J _{SC}	1069	23.0	72.6	17.8
			J _{SC} to Voc	1006	23.0	64.2	14.8
C ₆₀ -anchored np-SnO _x	1. 61 eV	0.1 cm ²	Voc to J _{SC}	1155	23.7	72.6	19.9
			J _{SC} to Voc	1065	23.7	68.2	18.4
a-NbO _x	1. 61 eV	0.1 cm ²	Voc to J _{SC}	1082	23.8	71.7	18.5
			J _{SC} to Voc	911	23.8	63.4	13.8
C ₆₀ -anchored a-NbO _x	1. 61 eV	0.1 cm ²	Voc to J _{SC}	1155	24.0	76.8	21.3
			J _{SC} to Voc	1158	24.0	75.8	21.1



Supplementary Fig. 14. Influence of the a-NbO_x thicknesses on the performance of the single-junction solar cells (1.61 eV). The statistical distribution of the device characteristics of the C₆₀-anchored a-NbO_x based devices with different a-NbO_x thicknesses, without cherry-picking from the batch. Note that, the reported devices here do not have 2D/3D passivation on perovskite layers.

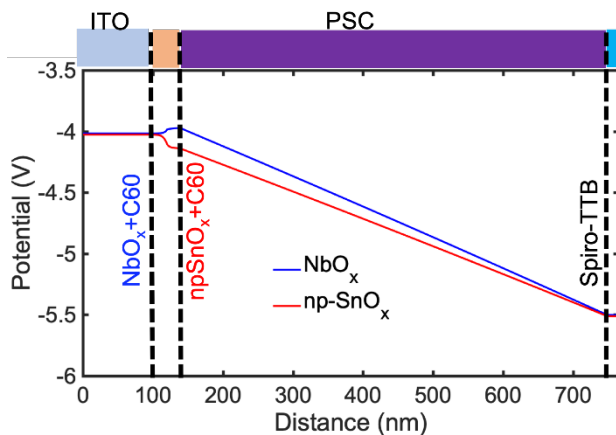
Supplementary Note 6: Electric-field simulation for the single-junction perovskite solar cells



Supplementary Fig. 15. Potential and electric field distribution on single-junction solar cells. Spatial distribution of the potential and **b**, the electrical field across the np-SnO_x, and **c, d**, across the NbO_x based PSCs. Here, PSC represents 1.61 eV perovskite, and Spiro describes Spiro-OMeTAD.

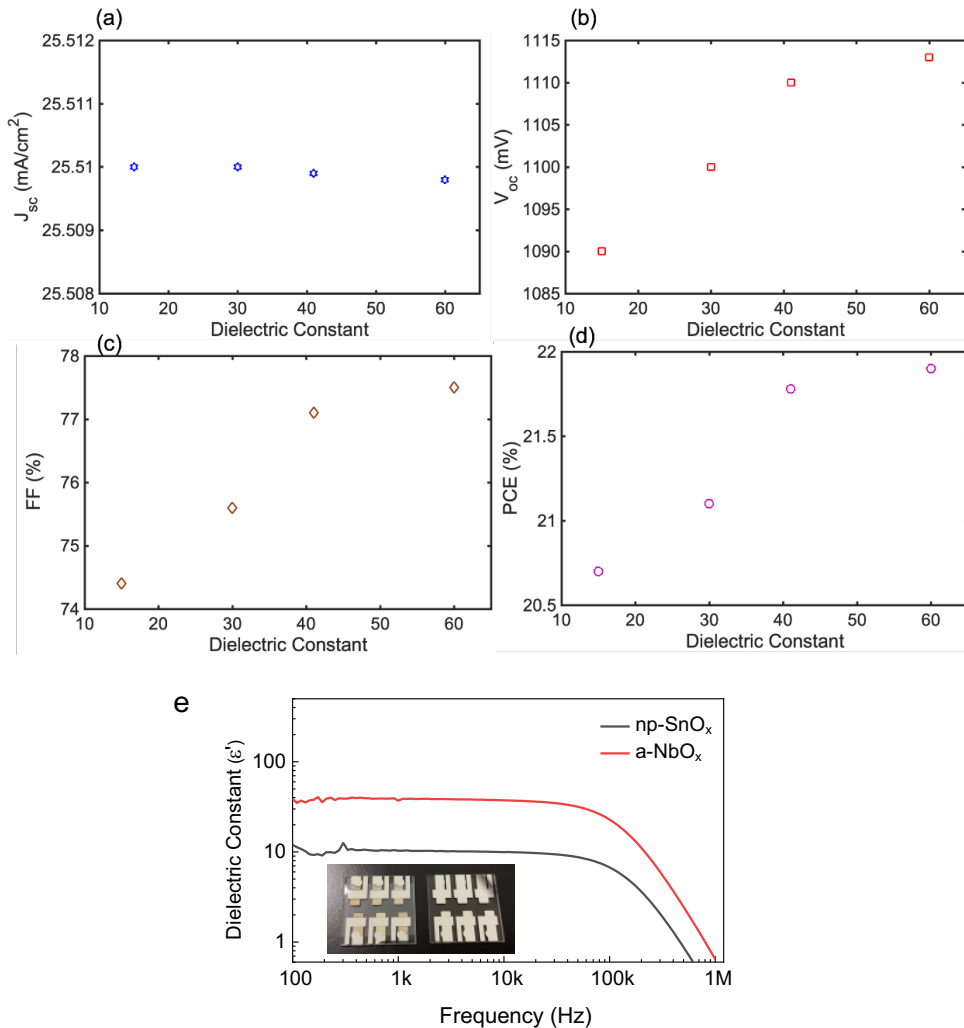
Supplementary Table 5. Parameters used for the simulations. Here, IL1 and IL2 represent the interface defect layers (for interfacial recombination) which were inserted ESL/perovskite and perovskite/HSL interfaces respectively. The thickness, and energetics (bandgaps, electron affinity) related to the perovskite and other layers used in the simulation are obtained from spectroscopic ellipsometry and UPS/IPES Measurement measurements and listed in **Supplementary Fig. S10** and **Table 3**. The dielectric constant (permittivity) at room temperature for a-NbO_x and np-SnO_x are measured by impedance spectroscopy. The Hall mobility of the a-NbO_x samples were out of range of the measurement tool so they were assumed same with np-SnO_x. Furthermore, other input parameters used in the simulation which are not included were set to be identical and consistent with previous simulations performed on perovskite solar cells ²⁶ : effective density of states at conduction (CB) and valence band (VB) were set to be 2.2×10^{18} and $1.8 \times 10^{19} \text{ cm}^{-3}$. The rest of the parameters are based on the literature values as given in the references.

Parameters	ITO	NbO _x	SnO _x	C ₆₀	IL1	PVK	IL2	Spiro-TTB
Thickness (nm)	120	50	20	2	5	600	5	25
Bandgap (eV)	3.06	3.85	3.9	2.45	1.68	1.68	1.68	3.44
e affinity (eV)	4.3	3.85	4.01	3.85	3.84	3.84	3.80	2.22
Permittivity (ϵ_r)	9.0 ⁽²⁶⁾	38.6	10.4	4.25 ⁽²⁷⁾	6.6	6.6 ⁽²⁶⁾	6.6	3.0 ⁽²⁸⁾
Mobility of e ⁻ (cm ² V ⁻¹ s ⁻¹)	20 ⁽²⁶⁾	0.34	0.34	0.16	5.31 ⁽²⁹⁾	5.31 ⁽²⁹⁾	-	-
Mobility of h ⁺ (cm ² V ⁻¹ s ⁻¹)	-	-	-	-	-	10.19 ⁽²⁹⁾	10.19	5.7×10^{-5} ⁽³⁰⁾
Density of n-type doping (cm ⁻³)	1.0×10^{19} ⁽²⁶⁾	1.3×10^9	9.3×10^{15}	1.0×10^{17}	1.0×10^{13}	1.0×10^{13}	1.0×10^{13}	-
Density of p-type doping (cm ⁻³)	-	-	-	-	-	-	-	1.0×10^{18} ⁽³¹⁾
Defects Density (cm ⁻³)	1.0×10^{15} ⁽²⁶⁾	1.0×10^{15}	1.0×10^{15}	1.0×10^{15}	1.0×10^{17} ⁽³²⁾	3.0×10^{11}	1.0×10^{17} ⁽³²⁾	1.0×10^{15}



Type	Bias	Peak 1	Peak 2	Peak1/Peak2
SnO _x	-1.0	3.25e6	4.01e6	0.80
	-0.5	2.42e5	3.01e6	0.81
	0.5	8.01e5	8.40e5	0.95
	1.0	2.10e5	1.50e6	0.14
NbO _x	-1.0	3.51e6	4.38e6	0.82
	-0.5	2.80e6	3.34e6	0.83
	0.5	1.28e6	1.20e6	1.06
	1.0	8.44e5	6.58e5	1.27

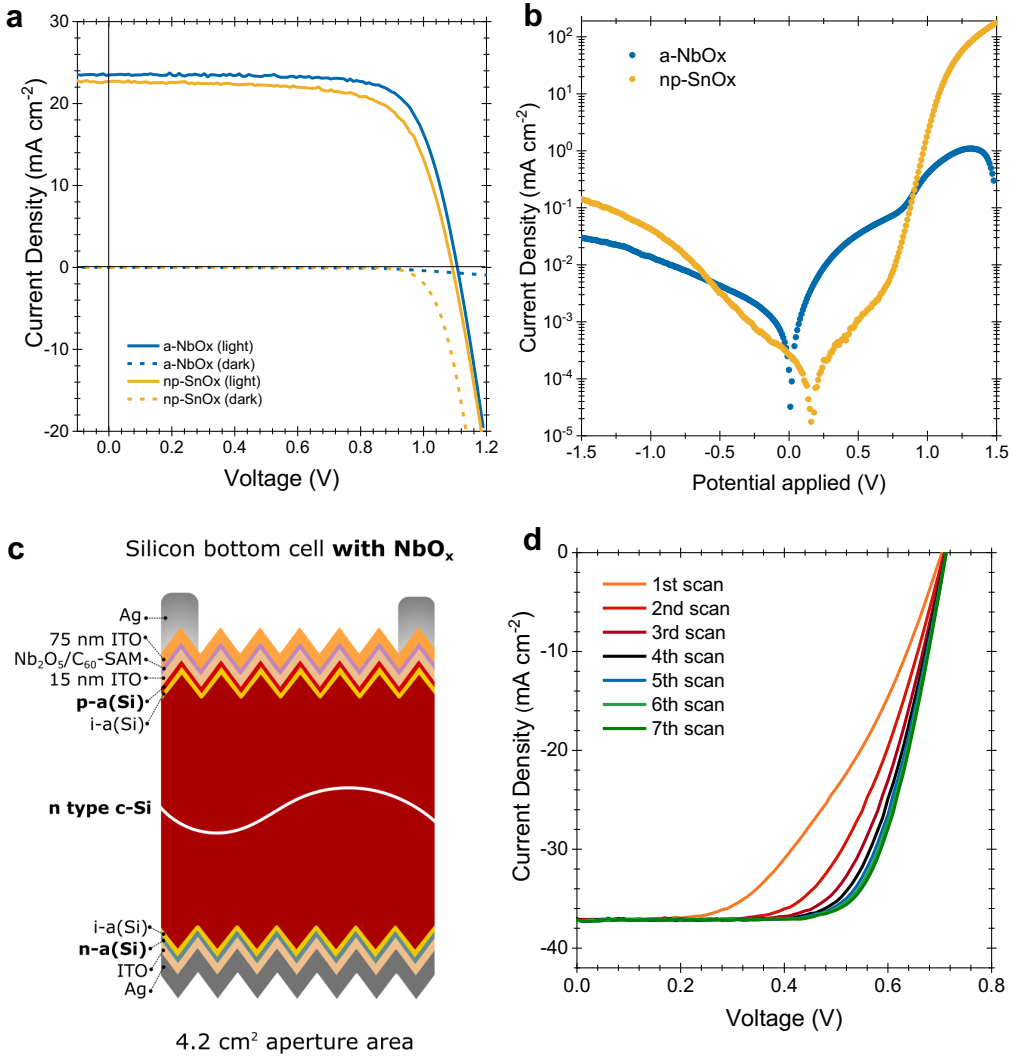
Supplementary Fig. 16. Comparison of potential distribution on the single-junction devices. Comparative analysis of potential distribution between NbO_x and the SnO_x PSCs at -0.5V (representative voltage) and summary of the peak ratios of the electric field at ESL/perovskite and perovskite/HSL interfaces.



Supplementary Fig. 17. Influence of the dielectric constant of ESLs on the device parameters. **a-d**, Simulated device parameters for PSCs as a function of the dielectric constant of the ESL. Increasing the dielectric constant of ESL results in increment on the FF and V_{OC} values. Therefore, one can attribute FF enhancement in a-NbO_x based PSCs to the high dielectric constant of a-NbO_x which is relatively higher than the np-SnO_x, as measured by impedance spectroscopy in panel e. The relative dielectric constant (ϵ') for both materials were calculated from complex impedance data using parallel plate capacitor model (for 20 nm SnO₂ and 50 nm Nb₂O₅ layers.), given by:

$$\epsilon' = \frac{t}{\omega A \epsilon_0} \cdot \frac{Z''}{Z'^2 + Z''^2}$$

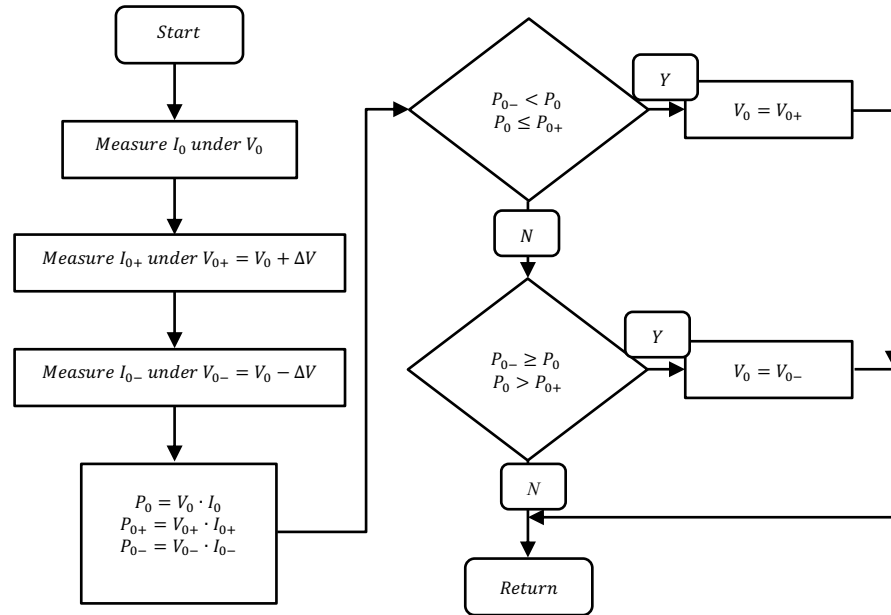
Here, A is the cross-section area of the parallel plate capacitor, t is the thickness of the individual layers, ϵ_0 is the permittivity of free space, ω equals $2\pi f$ (f is the frequency of operation), Z' is the real part and Z'' is the imaginary part of the complex impedance data.³³ The dielectric constant of the thin films remained constant for both materials in from 100 to 50 kHz. A picture of the stacks used for measurements (Ag/a-NbO_x/Ag, and Ag/np-SnO_x/Ag) are shown in the inset.



Supplementary Fig. 18. a-NbO_x enables higher FF values compared to np-SnO_x ESLs. **a**, Light and dark J – V curves for the PSCs based on a-NbO_x and np-SnO_x based ESLs. **b**, Semilog dark J – V curves of the devices. **c**, Si test cell, and **d**, corresponding J – V curves with different J – V scan cycles. Interestingly, we observed that applying a voltage bias to the silicon test cells with a-NbO_x interlayer enhances the FF of the devices. The increased passivation effect of the light-soaked a-NbO_x ESL was observed previously for silicon solar cell applications.³⁴ The mechanism, in general, explained by increasing excess electron density by light was likely to be injected or tunneled into trap states in the oxide film and increased level of field-effect passivation.^{35, 36} In line with this, the J – V characteristics of our devices confirm this behavior. Although np-SnO_x based devices show ideal diode behavior, the dark J – V of the a-NbO_x based devices show different behavior and forms a crossover with the light J – V curves, which confirms light-induced enhancement of the diode behavior. Our TRPL measurements further confirm the field-effect passivation of the a-NbO_x films by showing enhanced PL lifetime, even higher than bare quartz glass substrates. PL lifetime of the np-SnO_x/perovskite stack is much lower than the quartz/perovskite stack.

Supplementary Note 7: Maximum power point tracking (MPPT) measurements algorithm

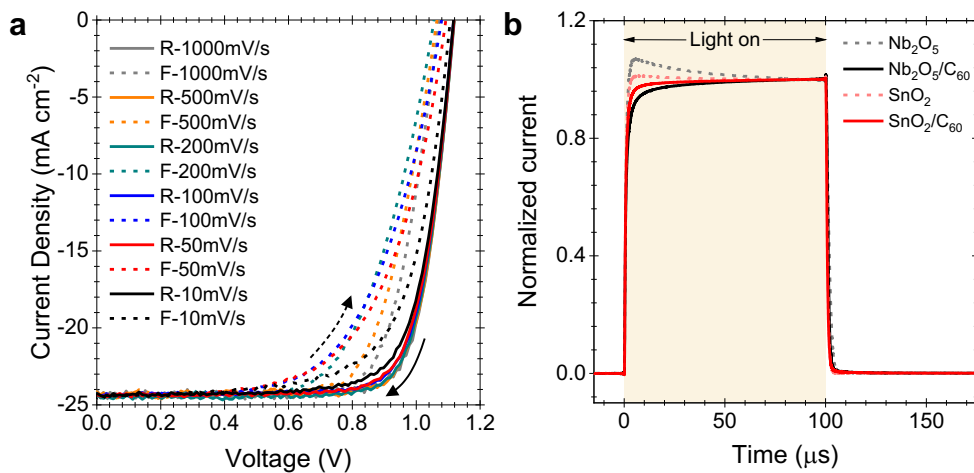
The stabilized power measurements have been recorded via the homemade LabView® based software using a three-point weight comparison method. The concept of this method is the same as that of ‘perturb and observe’ (P&O); that is, the MPPT is realized by observing the power change induced by a perturb voltage.³⁷ The difference is, our method uses two perturb voltages (**Supplementary Fig. 19**), and so we have three power points to weigh the power changes. This method can avoid the unnecessary change of the operation voltage when solar radiation is varying quickly or when data reading error occurs.³⁸



Supplementary Fig. 19. Algorithm for MPP measurements. Algorithm for three-point weight comparison.

Supplementary Note 8: Interpretation of hysteresis behavior

The hysteretic behavior of our devices when the voltage scan direction changes can be due to several reasons: (i) the charge accumulation at the ESL/perovskite interface due to the potential barrier induced by the high CBM offsets, (ii) trap states at the interfaces, (iii) migration of the charged ion through the interface under electric field due to the defects within the perovskite, (iv) the change of the surface chemistry of the perovskite layer after deposition on ESLs, as a characteristic of the chosen composition.³⁹⁻⁴¹ Here, based on our UPS/IPES measurements, there is no potential barrier at C₆₀-anchored a-NbO_x/perovskite (1.61 eV) contacts. Low bulk conductivity of the a-NbO_x may also cause unbalanced charge extraction at the contacts and causes hysteresis behavior. This problem has been fixed in the TiO₂ case by utilizing the mesoporous scaffold, which increases the surface area and provides efficient charge extraction. Here, this effect can be minimized by the doping of a-NbO_x layers as a future study. To shed more light on the hysteresis phenomenon, we performed transient photocurrent (TPC) measurements on the a-NbO_x- and np-SnO_x-based devices with and without C₆₀-anchoring. Pristine a-NbO_x shows a clear overshoot in the TPC transient, which is commonly attributed to complications in the charge extraction, such as charge accumulation at the a-NbO_x/perovskite interface. This phenomenon is suppressed in the pristine np-SnO_x sample. However, after C₆₀-anchoring, the current overshoot is eliminated for both a-NbO_x and np-SnO_x samples, suggesting an improved extraction induced by the presence of C₆₀.⁴⁰ As presented in **Supplementary Fig. 20**, the hysteresis index (HI) of the devices decreases with both decreasing and increasing the scan speed. TPC measurements confirm also the fast stabilization of the P_{MPP} values (within the microseconds regime). We fully eliminated the hysteresis on the devices by utilizing urea additive and iBAI:FAI 2D/3D mixed surface passivation of the devices, as discussed in **Supplementary Fig. 30**.

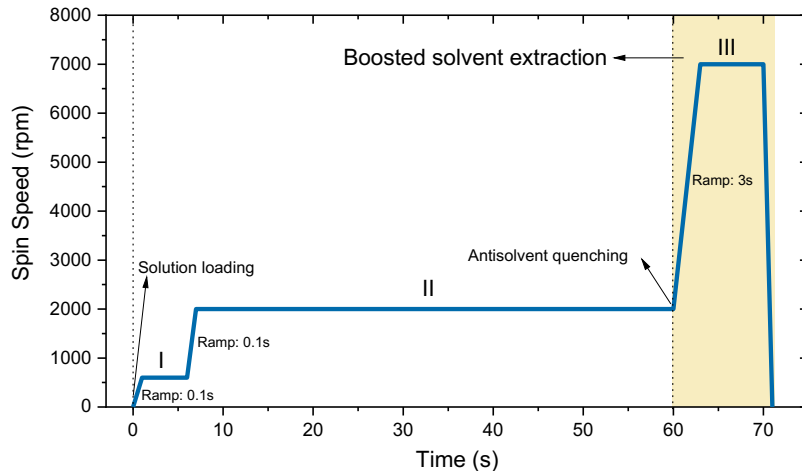


Supplementary Fig. 20. Hysteresis analysis of single-junction solar cells. **a**, Influence of the voltage scan speed on the hysteresis behavior of the C₆₀-anchored a-NbO_x based PSCs based on 1.61 eV perovskite absorbers. **b**, Transient photocurrent behavior of the devices measured with a white LED and a 100 μs square pulse. Here the measurements are performed on the device stack shown in Figure 2a. According to the J-V characteristics, our devices demonstrate normal hysteresis.^{42, 43}

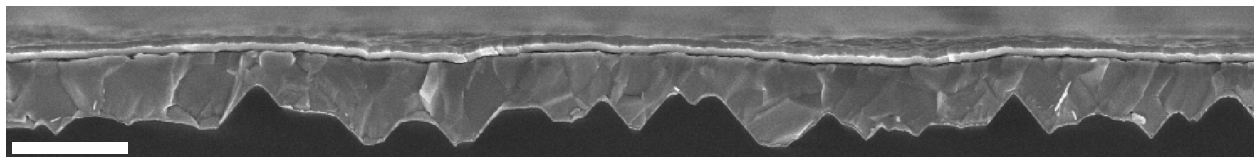
Supplementary Note 9: Fabrication of micrometer-thick perovskite absorbers on textured interfaces

Processing perovskite films on rough surfaces via solution-based techniques was a great challenge in the community. The main obstacle was achieving well-covered interfaces since the randomly oriented surface features (pyramids in c-Si bottom cell case) was contacting with top electrodes and was causing shunt problems. In our recent study, we demonstrated the processability of the spin-coating technique on textured interfaces.⁴⁴ Here, additionally, we utilize the combination of *boosted solvent extraction* (BSE) technique, which is reported by Chen et al.⁴⁵ **Supplementary Fig. 21a** plots the spin-coating recipe used for the fabrication of perovskite layers. One of the key enablers forming pin-hole free and continuous films is using the reduced average pyramids size to the 1-2 mm range as defined in the previous study.⁴⁴ BSE technique enables a homogeneous and smooth morphology in perovskite films having a large crystal, as shown in the SEM cross-section image in **Supplementary Fig. 21b**, and enhanced diffusion length.⁴⁵ Importantly, the high concentration of the perovskite precursor ink is another key enabler of such thick films at high quality together with the BSE technique. Note that depending on the surface energy of the underlying layer, the second step in the spinning recipe can be altered by increasing (for low surface energy) or decreasing (for high surface energy) the processing window of the second step.

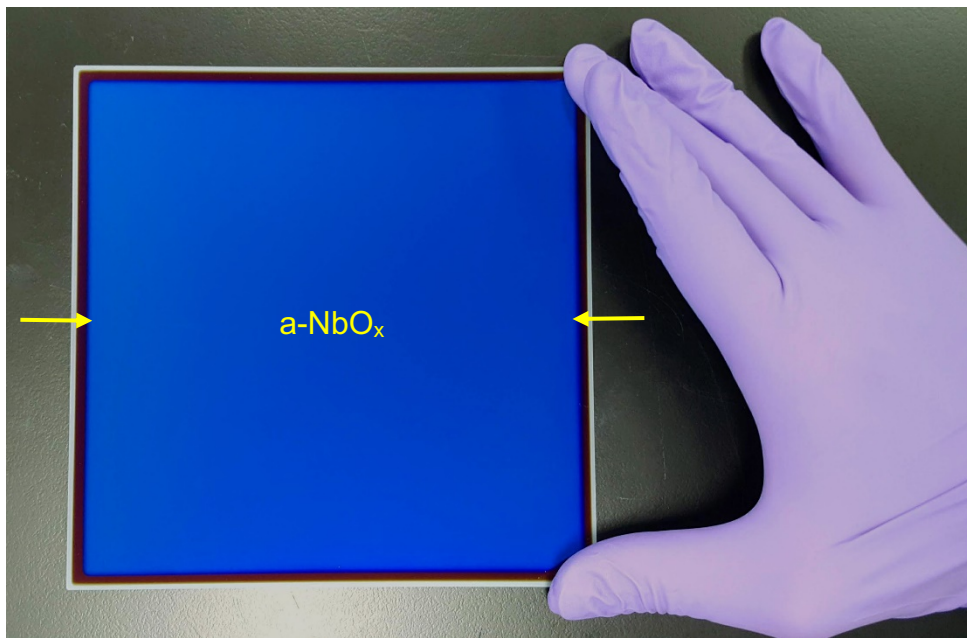
a



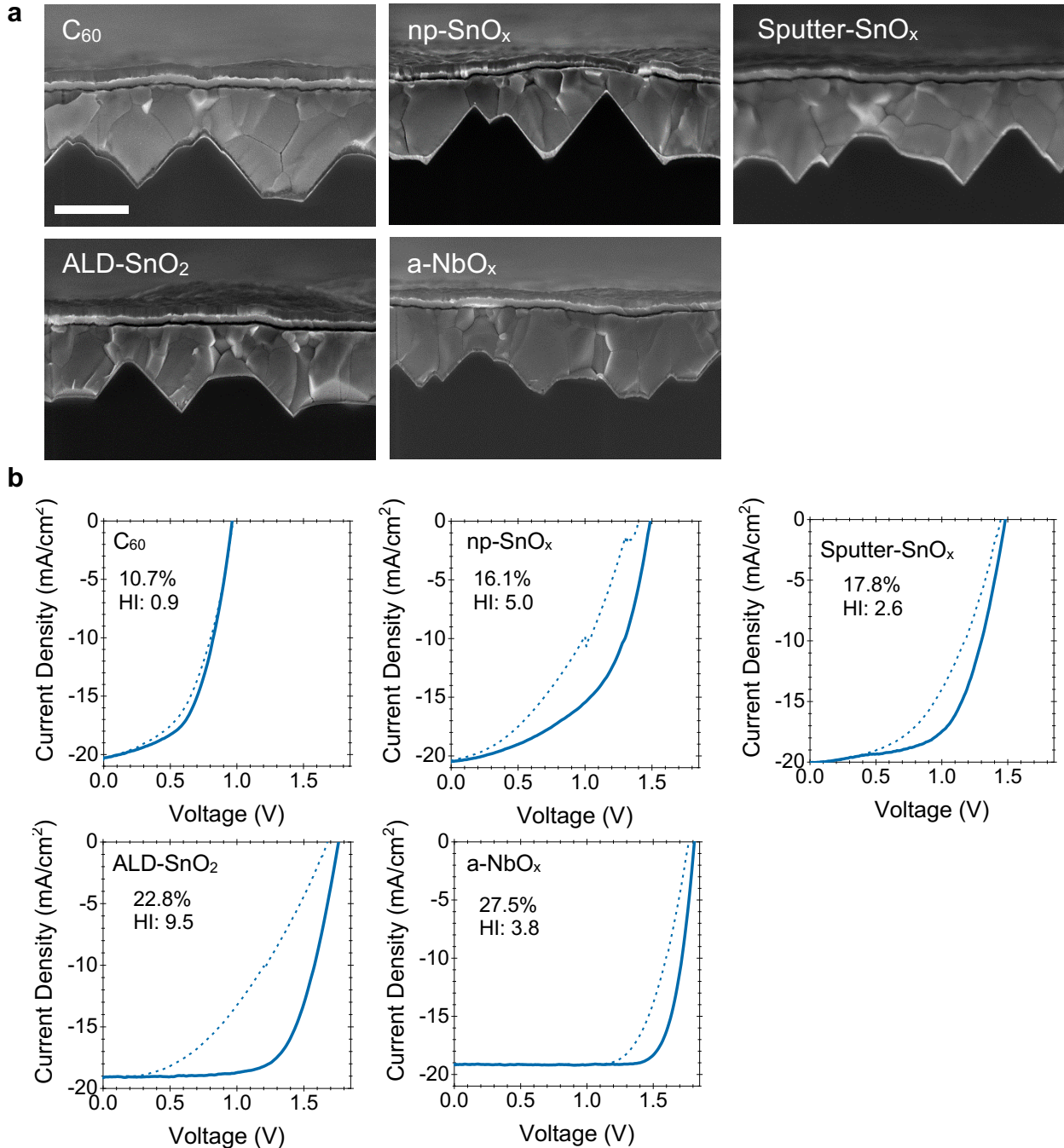
b



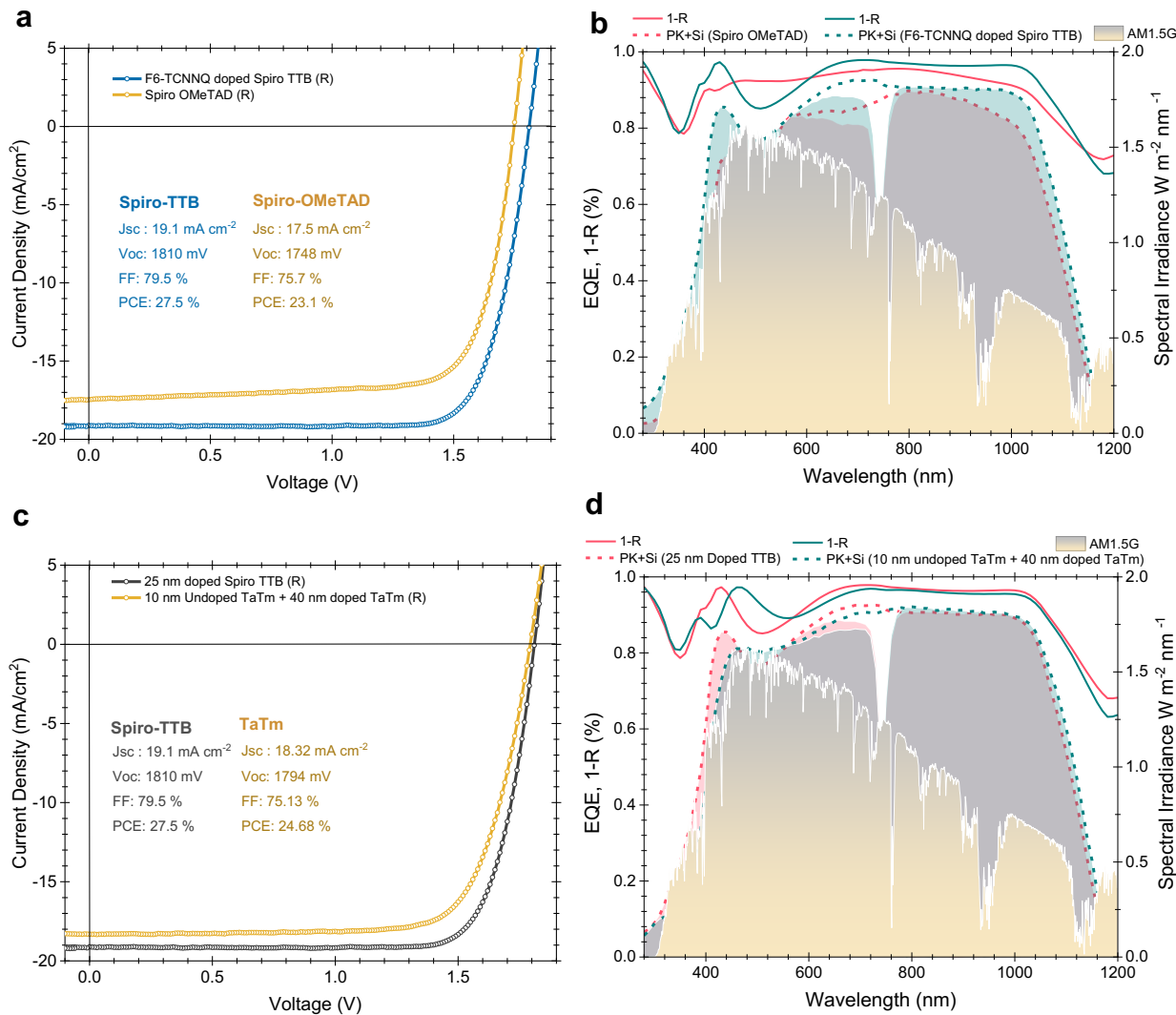
Supplementary Fig. 21. Deposition protocol of perovskite layers on textured substrates. a, Spin coating recipe of the perovskite absorbers on textured c-Si bottom cells. **b,** Cross-section SEM image of the full-device stack on textured c-Si bottom cells. The white bar is 2mm.



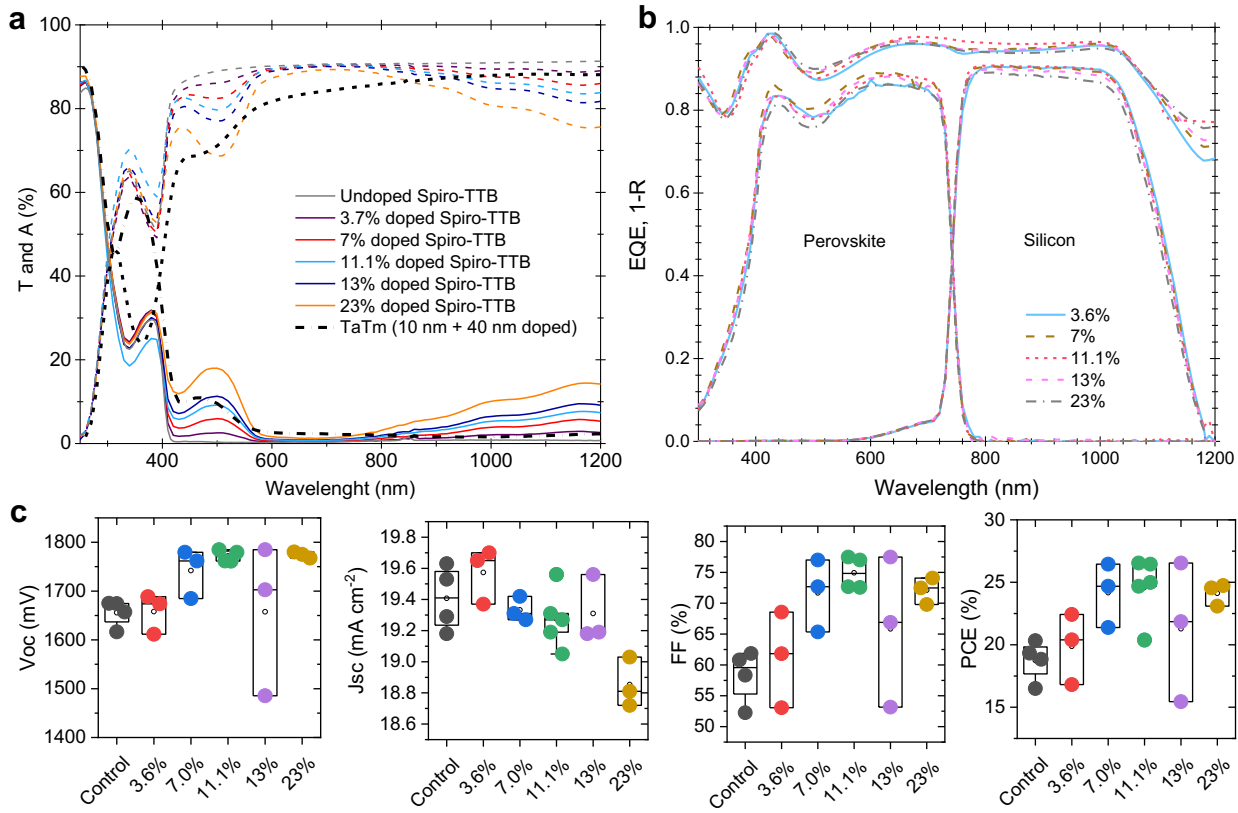
Supplementary Fig. 22. Large area deposition of a-NbO_x films on commercial silicon solar cells. The picture of the 20 nm a-NbO_x films (blue colored region) on a 6-inch commercial SHJ solar cell, which is clearly showing the large-scale fabrication potential of the sputtered a-NbO_x layers. The flagged blue area presents the a-NbO_x layer. Processing of the thin-film components of the tandem solar cell up to a 6-inch wafer scale is a critical step to get the full benefits of the well-established c-Si technology. For this, scalable and industry compatible techniques should be considered for the fabrication of such layers, such as sputtering. Previously, we reported nanocrystalline NiO_x hole transport layers⁴⁶ with RF sputtering, which is now widely used for *p-i-n* configuration tandem solar cells.^{44, 47} Here, for *n-i-p* based tandems, we developed a-NbO_x films with the same technique. The photograph of the a-NbO_x films on textured-commercial SHJ solar cells which shows the high homogeneity of the films over a large area.



Supplementary Fig. 23. Comparison of various ESLs on tandems without 2D/3D passivation. **a**, SEM top-view images and **b**, J - V characteristics of the devices on various ESLs. The scale bar is 1 mm. The thickness of the thermally evaporated C_60 is 20 nm, atomic layer deposited SnO_x is 20 nm,⁴⁸ sputtered SnO_x is 17 nm,²¹ np- SnO_x is around 20-50 nm²⁵ (varies at profile due to the inhomogeneous deposition of np- SnO_x). We should note that C_60 ESL-based devices resulted in shunt behavior, due the potential dissolution during the perovskite processing. Note that, the devices here are identical apart from the ESLs. All ESL are modified by C_60 -SAM.



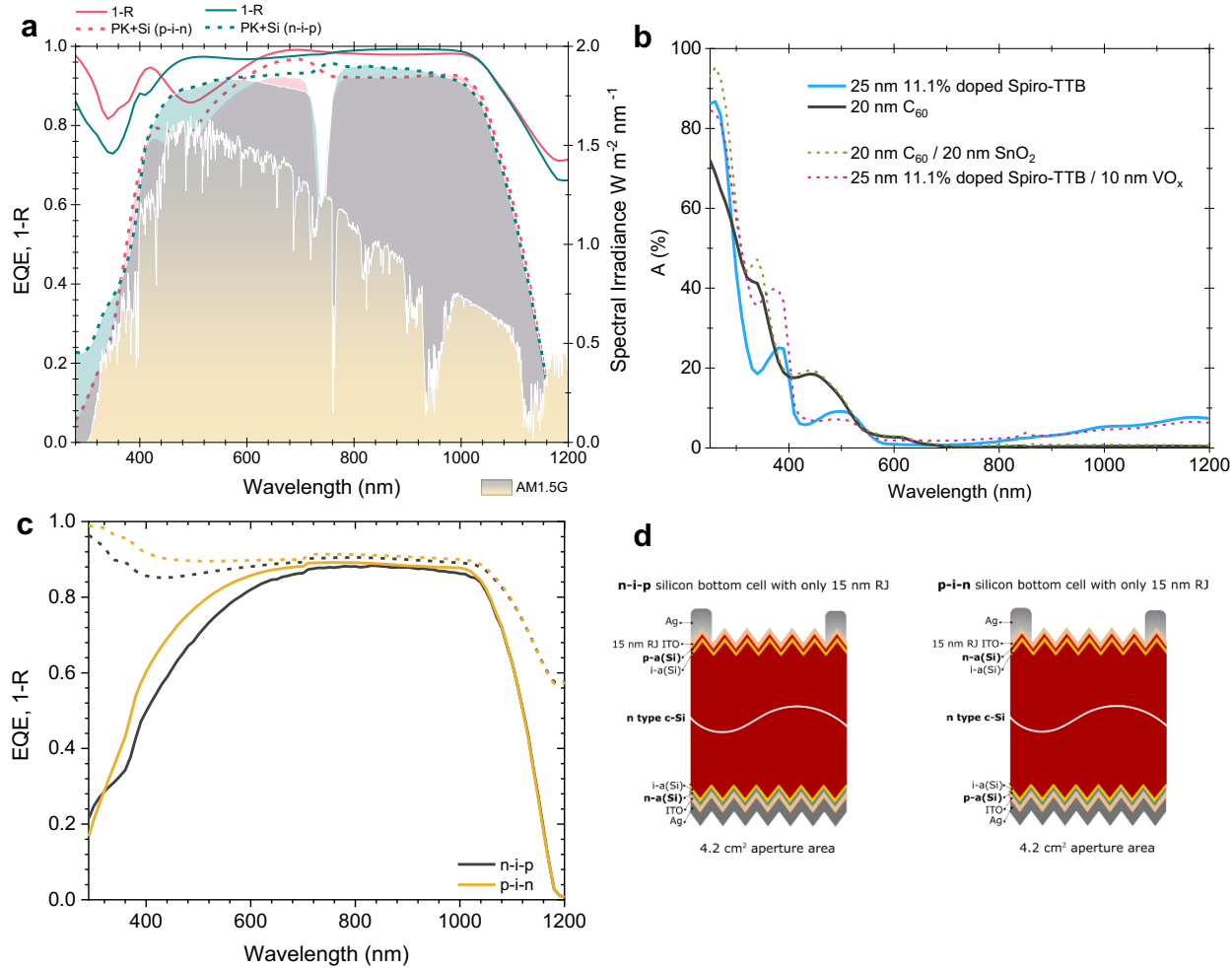
Supplementary Fig. 24. Comparison of various HSLs on tandem solar cells. **a,** $J-V$ and **b**, EQE comparison of the tandem devices based on Spiro-OMeTAD and F6-TCNNQ doped Spiro-TTB HSL. **c,** $J-V$ and **d**, EQE comparison of F6-TCNNQ doped Spiro-TTB and TaTm HSLs. Note that for fair comparison, both devices utilize 100 nm front IZO and 170 nm rear ITO, and the perovskite layers are not passivated by iBAI:FAI. R represents the reverse scan.



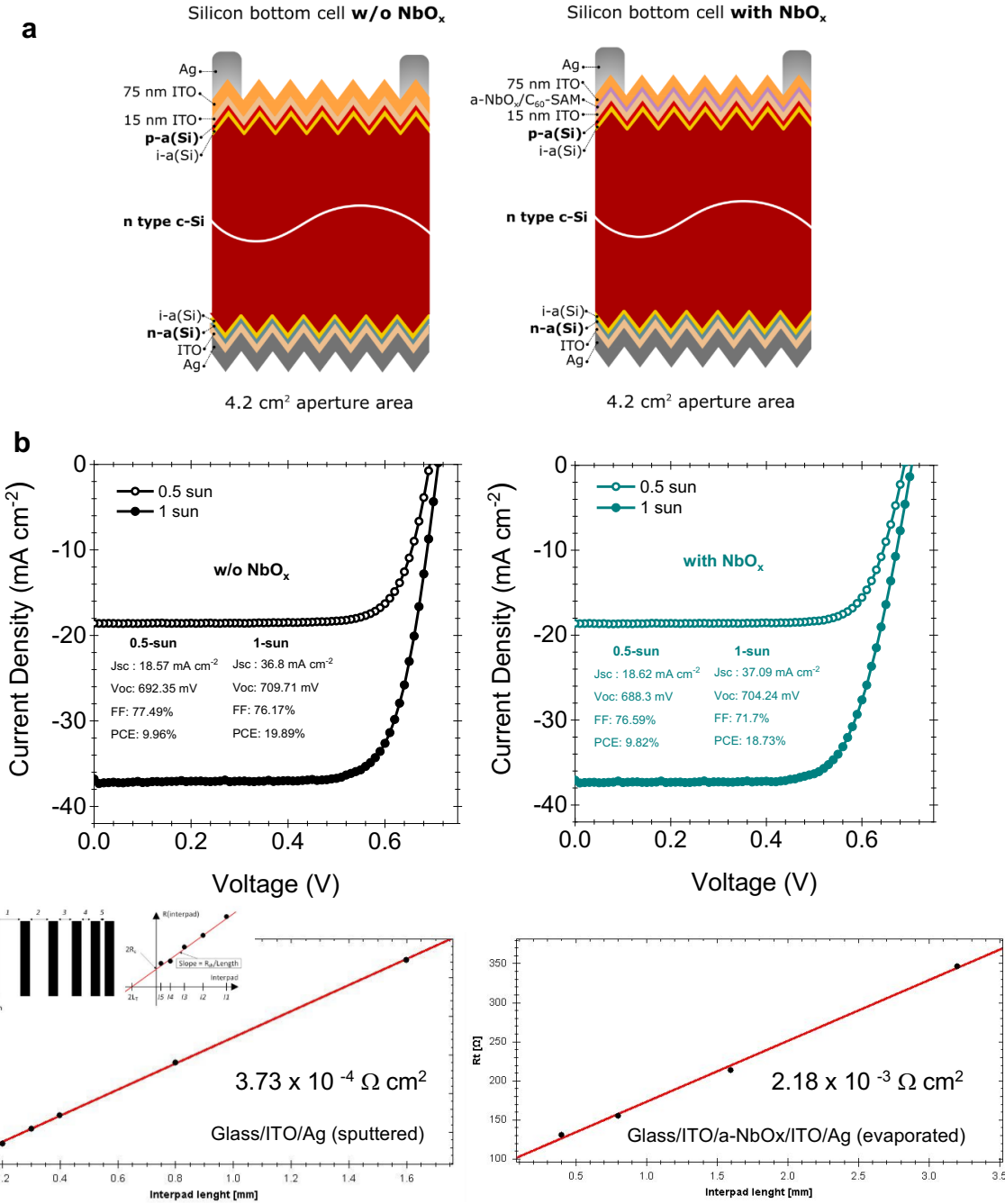
Supplementary Fig. 25. Optimization of F6-TCNNQ doping of spiro-TTB for tandems. **a**, Optical transmittance (T , dashed lines) and absorptance (A , continuous lines) spectra of the F6-TCNNQ doped spiro-TTB and TaTm layers. **b**, EQE spectra, and **c**, device statistics of the tandems based on doped Spiro TTB layers. Here, the devices were fabricated in the same batch, and the results were reported without any cherry-picking. Note that for fair comparison, all devices utilize 100 nm front IZO and 170 nm rear ITO as transparent electrodes, and the perovskite layers are not passivated by iBAI:FAI.

Supplementary Note 11: Comparison of *n-i-p* and *p-i-n* tandem solar cells

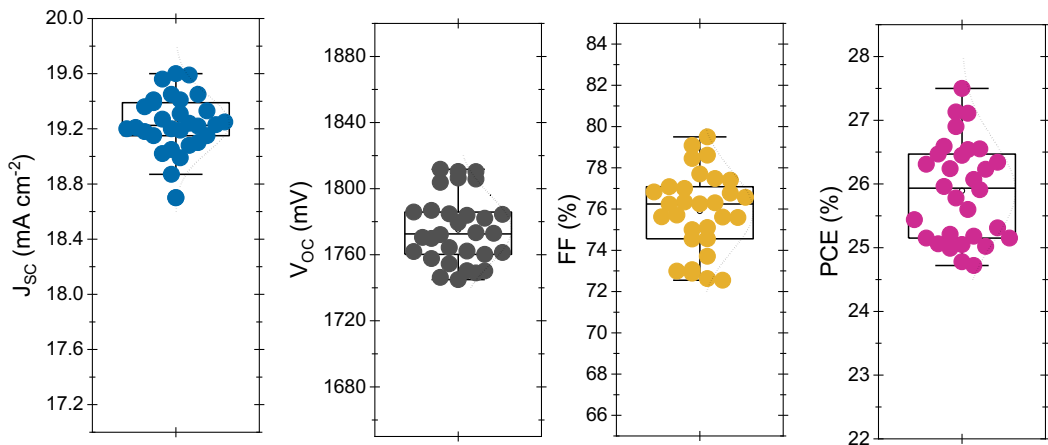
Here, we reported the EQE and 1-R results for the optimized device configurations of *n-i-p* and *p-i-n* devices. The *p-i-n* configuration devices were fabricated as shown in Ref.⁴⁴ The EQE losses at NIR region of *n-i-p* devices is due to the parasitic absorption originating from the doped Spiro TTB. As can be seen in **Supplementary Fig. 26.b**, spiro-TTB/VOx contacts cause less parasitic absorption in the blue region than C₆₀/SnO_x contacts. Both *n-i-p* and *p-i-n* SHJ subcells show similar NIT responses.



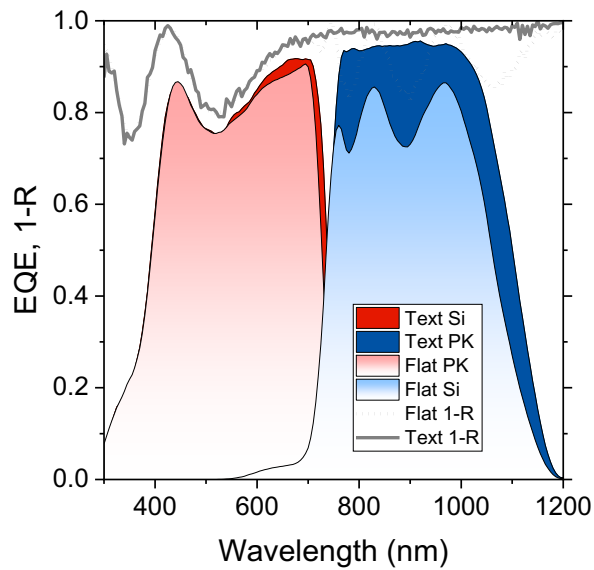
Supplementary Fig. 26. Comparison of *n-i-p* and *p-i-n* tandem solar cells. **a**, EQE comparison of *p-i-n* and *n-i-p* configuration tandems fabricated with 20 nm C₆₀/20 nm ALD SnO₂/100 nm IZO contacts and 25 nm F6-TCNNQ doped Spiro-TTB/12 nm ALD VO_x/100 nm IZO contacts, respectively. **b**, Absorptance (A) spectra comparison of 20 nm C₆₀ and 25 nm F6-TCNNQ doped Spiro-TTB contacts. **c**, EQE, and 1-R (dotted lines) spectra of the *n-i-p* and *p-i-n* bottom cells with only 15 nm RJ ITO layer and with printed metal fingers. **d**, The architecture of the devices used for EQE measurements in panel c.



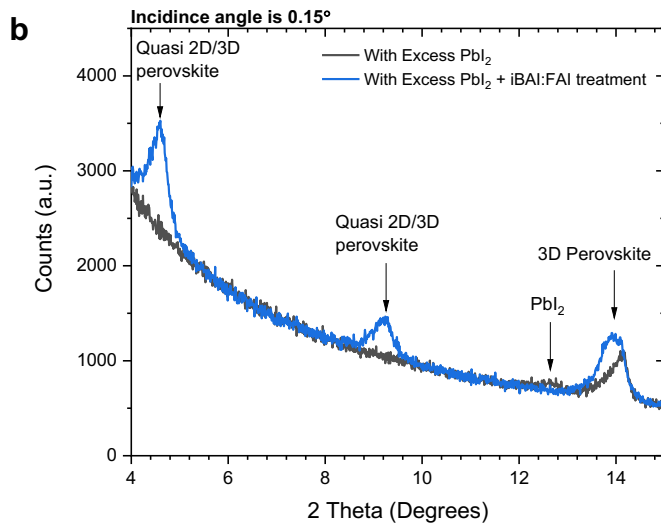
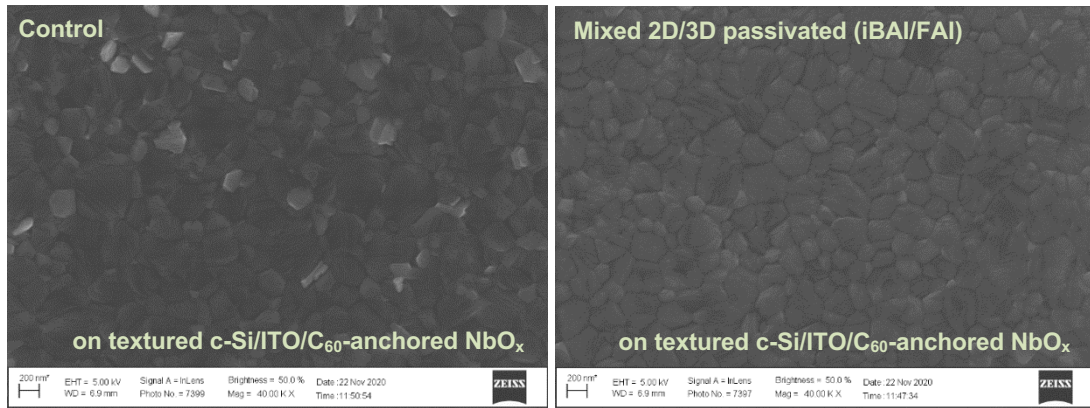
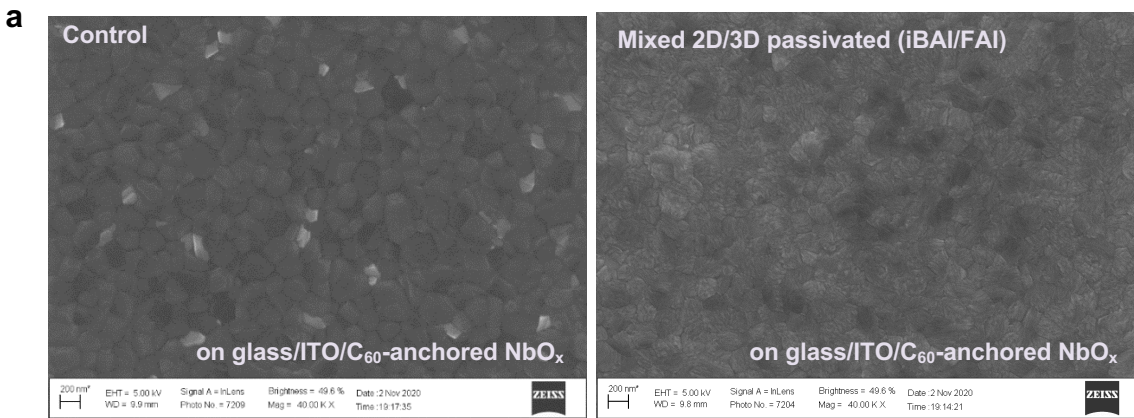
Supplementary Fig. 27. Performance analysis of *n-i-p* silicon bottom cells. **a**, Device architecture of the SHJ bottom cells and recombination junction test structures and **b**, corresponding J - V characteristics. The test devices were fabricated on the same wafer used for the tandem devices, and the front side is metalized by screen-printed metal fingers. Here, although it's insulating nature, a- NbO_x does not bring considerable resistive losses at 0.5 suns. **c**, Contact resistivity results from transmission line measurement (TLM).



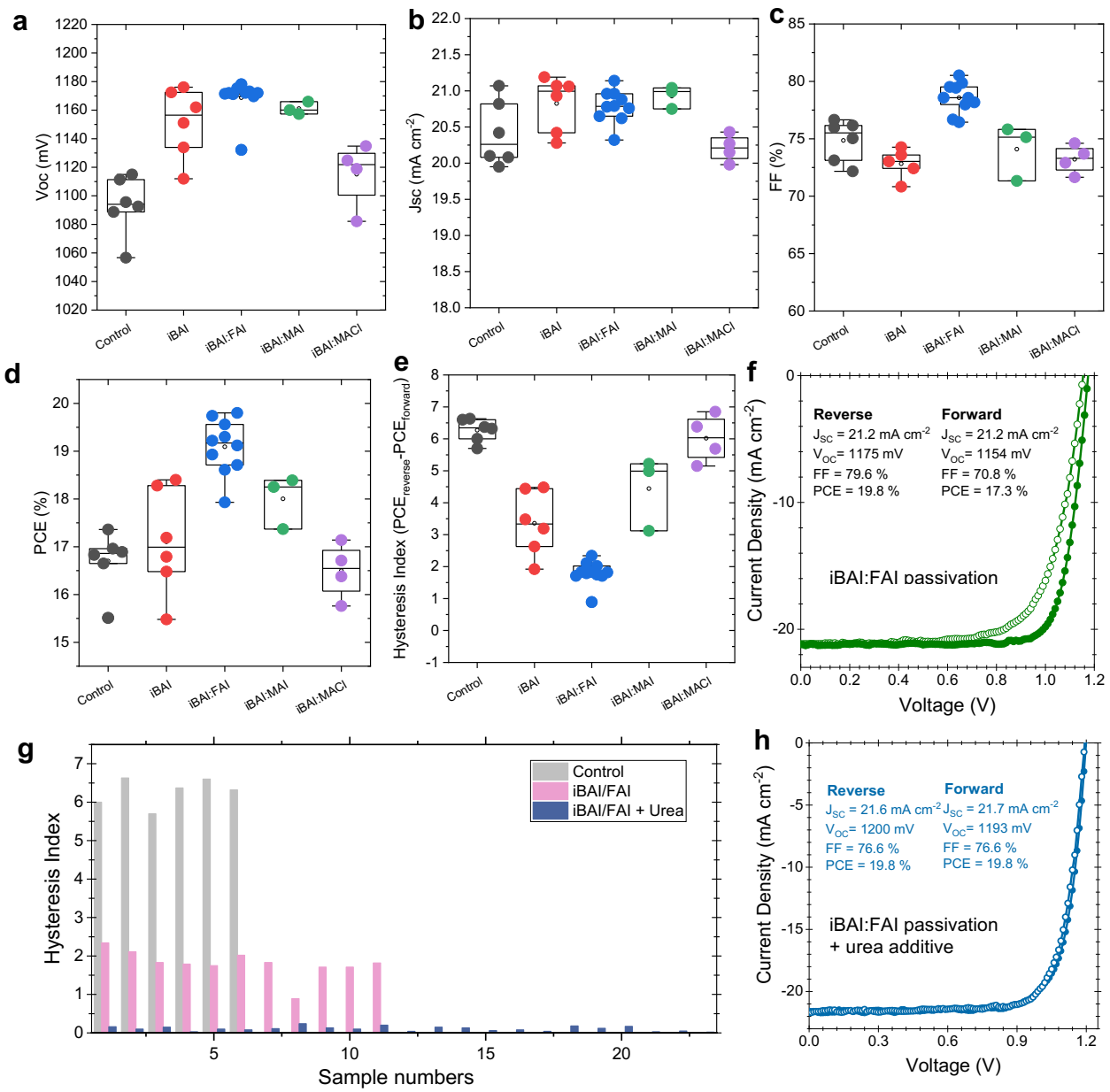
Supplementary Fig. 28. Device statistics of the perovskite/silicon tandems based on C_{60} -anchored a-NbO_x . Device statistics for 30 devices over 5 subsequent batches. Note that the given device parameters represent the J - V measured data (for the reverse scan) after 5 minutes of MPP tracking.



Supplementary Fig. 29. Optical simulation for the perovskite/silicon tandem solar cells.
 SunSolve EQE and 1-R simulation results for the rear side textured and double-side textured perovskite/silicon tandem solar cells. For the rear-side-textured devices, interference fringes at the near-infrared part are originating due to the front reflection of the devices. Double-side-texturing maximizes the light coupling at this part of the spectrum by minimizing the reflection.



Supplementary Fig. 30. Mixed 2D/3D passivation of wide bandgap perovskites. **a**, SEM cross-section images of 1.68 eV perovskite layers on glass/ITO/C₆₀-anchored a-NbO_x and textured c-Si/ITO/C₆₀-anchored a-NbO_x substrates for before and after mixed 2D/3D passivation. **b**, GIXRD of the perovskite layers with and without 2D/3D passivation. Here, the perovskite layer has 10 mM excess PbI₂ inside the precursor solution. By applying this passivation, iBAI assists the formation of crystalline perovskite phase when FAI reacts with the excess PbI₂.



Supplementary Fig. 31. Single-junction perovskite solar cells based on mixed 2D/3D passivation of 1.68 eV perovskites. **a-d**, Device statistics of single junction devices for various organic cations mixtures. **g**, The distribution of the hysteresis index of the single junction devices with various cation mixtures. **f**, Representative J - V curve for iBAI:FAI passivated single-junction devices. Note that the concentration of the solution was 10 mM and the iBAI:cation ratio was 3:1 by weight. **g**, The distribution of the hysteresis index of the devices before and after urea additive, and **h**, representative J - V curve for both iBAI/FAI passivated and urea additive applied devices.

Supplementary Table 7. Summary of the perovskite/silicon tandem solar cells in the literature. Here the devices are categorized according to used ESL and HSL materials and used bottom cells.

***n-i-p* configuration**

Perovskite Absorber (Aperture area)	ESL	HSL	Buffer Layer	Bott om Cell	Scan Direction	Voc (V)	Jsc (mA cm ⁻²)	FF (%)	PCE (%)	Stability	Year	Ref.
Silicon heterojunction bottom cells												
MAPbI ₃ (1.43 cm ²)	<i>PCBM</i>	Spiro-OMeTAD	MoO _x	RST	Voc to Jsc	1718	16.4	70.0	19.7	n/a	2016	49
					Jsc to Voc	1717	16.4	73.1	20.6			
FAMAPbI _{3-x} Br _x (0.16 cm ²)	<i>SnO₂</i>	Spiro-OMeTAD	MoO _x	DSP	Voc to Jsc	1785	14.0	79.5	19.9	n/a	2016	50
					Jsc to Voc	1759	14.0	77.3	19.1			
MAPbI ₃ (0.17 cm ²)	<i>PCBM</i>	Spiro-OMeTAD	MoO _x	DSP	Voc to Jsc	1690	15.9	77.6	20.9	n/a	2016	51
					Jsc to Voc	1692	15.8	79.9	21.4			
Cs _x MA _{1-x} PbI ₃ (1.43 cm ²)	<i>C₆₀</i>	Spiro-OMeTAD	MoO _x	RST	Voc to Jsc	1777	16.5	74.4	21.8	n/a	2017	52
					Jsc to Voc	1779	16.5	74.1	21.7			
CsFAMAPbI _{3-x} Br _x (0.13 cm ²)	<i>SnO₂</i>	Spiro-OMeTAD	MoO _x	DSP	Voc to Jsc	1830	16.0	70.0	20.4	n/a	2019	53
					Jsc to Voc	1810	16.0	69.0	20.0			
CsFAMAPbI _{3-x} Br _x (1.03 cm ²)	<i>a-NbO_x</i>	Spiro-TTB	TPBI/VO _x	DST	Voc to Jsc	1828	19.5	75.9	27.1	T ₉₀ , 150h	2020	T.W.
					Jsc to Voc	1837	19.5	72.5	26.0			
Homo-junction silicon bottom cell												
FAMAPbI _{3-x} Br _x (4 cm ²)	<i>SnO₂</i>	Spiro-OMeTAD	MoO _x	DSP	Voc to Jsc	1676	16.1	78.0	21.0	n/a	2018	54
					Jsc to Voc	1688	16.2	70.0	19.1			
FAMAPbI _{3-x} Br _x (4 cm ²)	<i>SnO₂</i>	Spiro-OMeTAD	MoO _x	RST	Voc to Jsc	1732	16.5	81.0	23.1	n/a	2019	55
					Jsc to Voc	1729	16.4	79.0	22.5			
FAMAPbI _{3-x} Br _x (4 cm ²)	<i>SnO₂</i>	Spiro-OMeTAD	MoO _x	RST	Voc to Jsc	1740	16.2	78	21.9	n/a	2018	56
					Jsc to Voc	1739	16.2	76	21.3			
Poly-silicon passivating contact silicon bottom cells												
CsRbFAMAPbI _{3-x} Br _x (1 cm ²)	<i>TiO₂</i>	PTAA	MoO _x	RST	Voc to Jsc	1763	17.8	78.1	24.5	n/a	2018	57
					Jsc to Voc	1735	17.8	77.7	24.0			

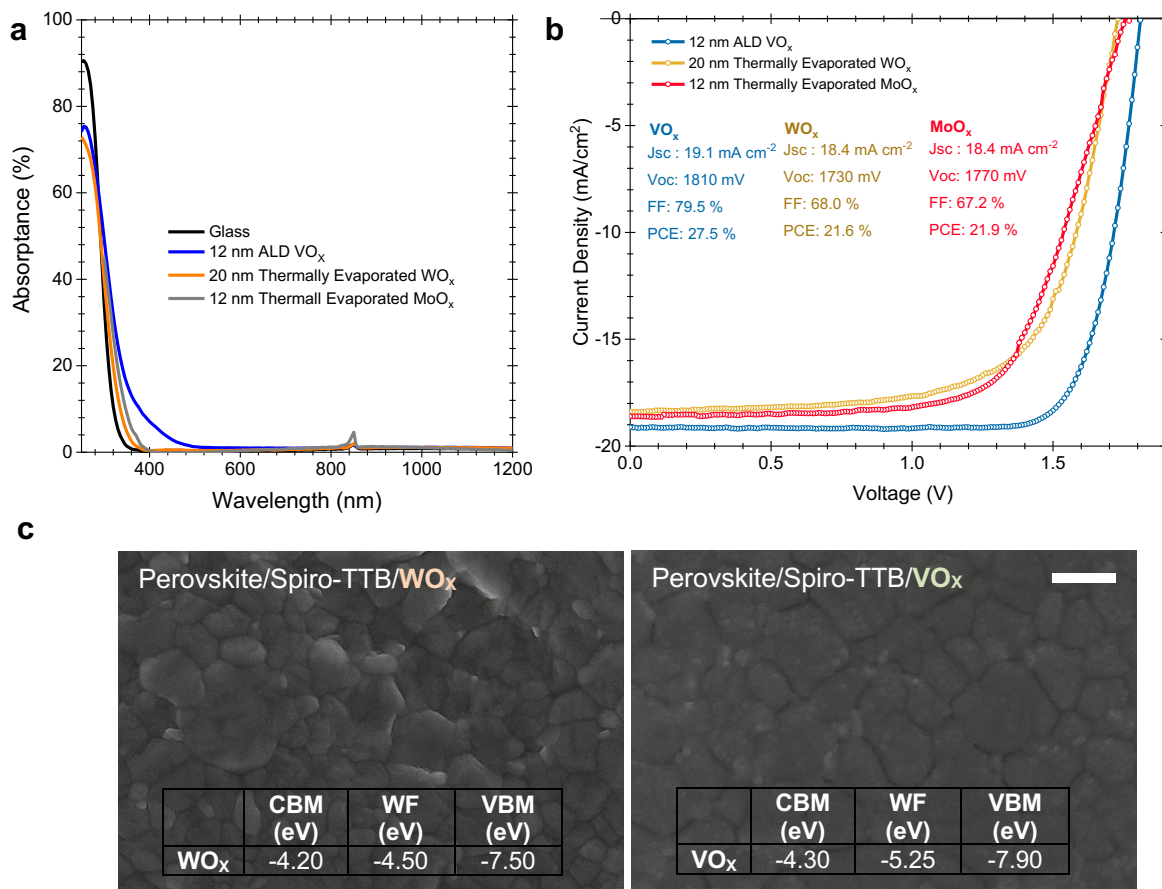
Champion *p-i-n* configuration devices published as of April 2021

Silicon heterojunction bottom cells												
CsFAPbI _{3-x} Br _x (1.03 cm ²)	<i>C₆₀</i>	Spiro-TTB	<i>SnO₂</i>	DST	Voc to Jsc	1735	19.8	73.1	25.1	Outdoor test	2020	58
					Jsc to Voc	1732	19.8	71.8	24.6			
CsFAMAPbI _{3-x} Br _x (1.03 cm ²)	<i>C₆₀</i>	<i>NiO_x</i>	<i>SnO₂</i>	DST	Voc to Jsc	1793	19.1	75.4	25.6	T ₉₀ , 400h	2020	44
					Jsc to Voc	1781	19.1	73.7	25.2			
CsFAPb(I _x BryCl _z) ₃ (1 cm ²)	<i>C₆₀</i>	<i>NiO_x/Poly-TPD</i>	<i>SnO₂</i>	RST	Voc to Jsc	1876	18.6	74.9	26.1	n/a for tandems	2020	47
					Jsc to Voc	n/a	n/a	n/a	n/a			
CsFAMAPbI _{3-x} Br _x (1 cm ²)	<i>C₆₀</i>	PTAA	PEIE	RST	Voc to Jsc	1818	19.4	76.4	26.2	n/a for tandems	2020	59
					Jsc to Voc	n/a	n/a	n/a	n/a			
CsMAPbI _{3-x} Br _x (n/a)	<i>C₆₀</i>	PTAA	<i>SnO₂</i>	DST	Voc to Jsc	1820	19.2	75.3	26.2	T ₉₀ , 100h	2020	60
					Jsc to Voc	1820	19.2	74.4	26.0			
CsFAMAPbI _{3-x} Br _x (1 cm ²)	<i>C₆₀</i>	MeO-4PACZ	<i>SnO₂</i>	RST	Voc to Jsc	1910	19.4	78.9	29.1	T ₉₀ , 300h	2020	61
					Jsc to Voc	1910	19.4	78.5	29.0			

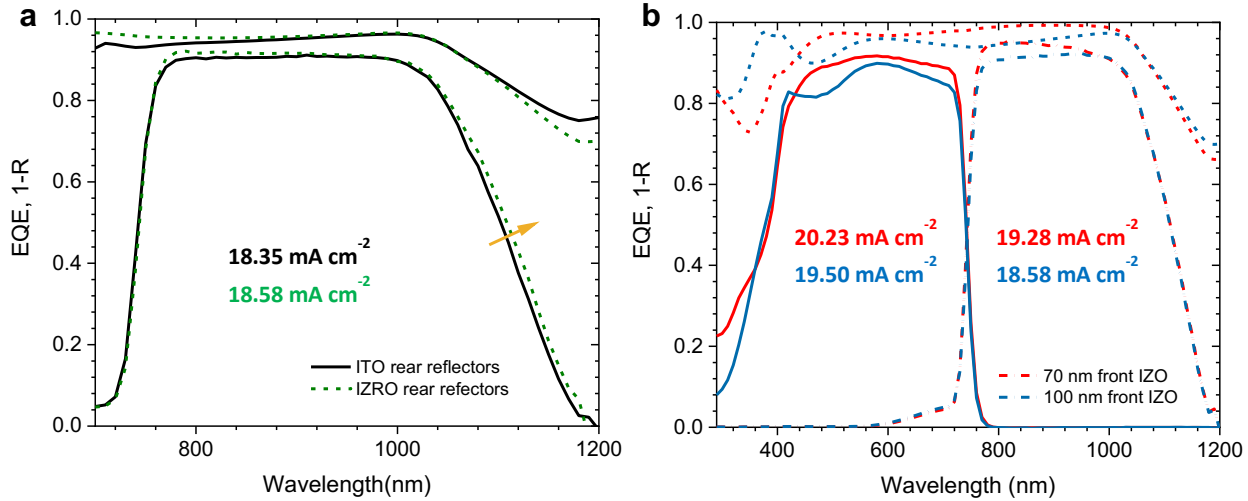
DSP: double side polished, RST: rear side textured, DST: double side textured, T.W: this work

Supplementary Note 13: Comparison of ALD deposited VO_x and thermally evaporated WO_x buffer layers

Transition metal oxides MoO_x ⁶², WO_x ⁶³, and VO_x ⁶⁴ good buffer layers to sputtering damage during the deposition of transparent conductive oxides on top of the soft layers such as organic ESLs and HSLs in addition to their exceptional electronic properties for charge injection and extraction in electronic devices.⁶⁵ Here, we choose ALD VO_x buffer layers on our tandems. As can be seen from top-view SEM images, ALD deposited 12 nm VO_x provides better coverage of the surface cracks and enables better FF values on the devices due to increased shunt resistance. Although evaporated 20 nm WO_x is more transparent (thinner films reduced the shunt resistance), its absorptance is screened by the spiro-TTB layer. In addition, WO_x brings contact resistivity problems. Therefore, for our tandem devices, we utilized ALD VO_x buffer layers.

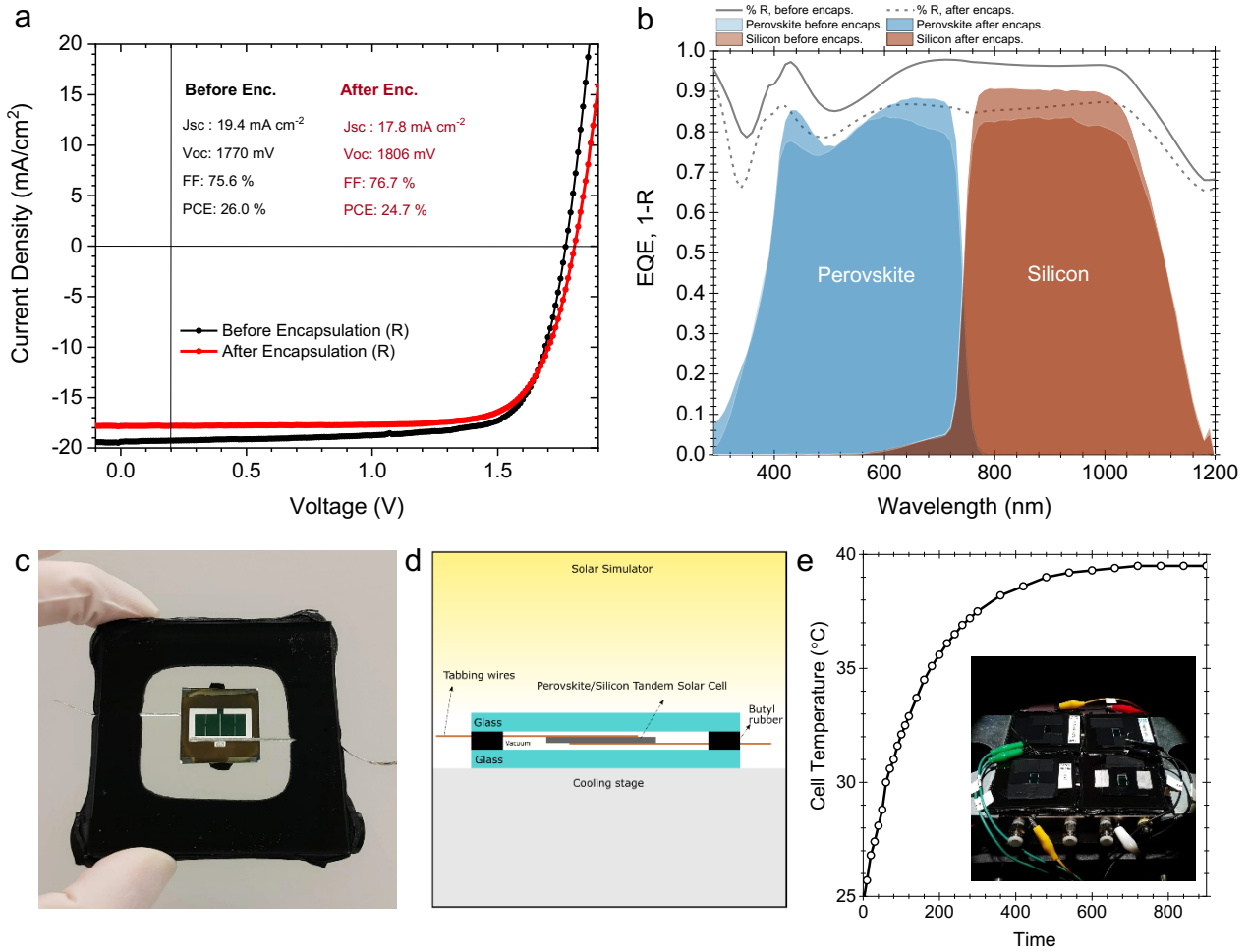


Supplementary Fig. 32. Choosing a protective buffer layers for tandems. **a**, Absorptance data for the thermally evaporated 20 nm WO_x , 12 nm MoO_x , and atomic layer deposited 10 nm VO_x films on soda-lime glass substrates. **b**, Corresponding reverse $J-V$ curves of the tandems. **c**, SEM top-view images of the perovskite grown on textured bottom cells. The inset values show the UPS analysis results of the 20 nm WO_x , and the atomic layer deposited 10 nm VO_x films on c-Si/ITO substrates. The white scale bar is 500 nm.

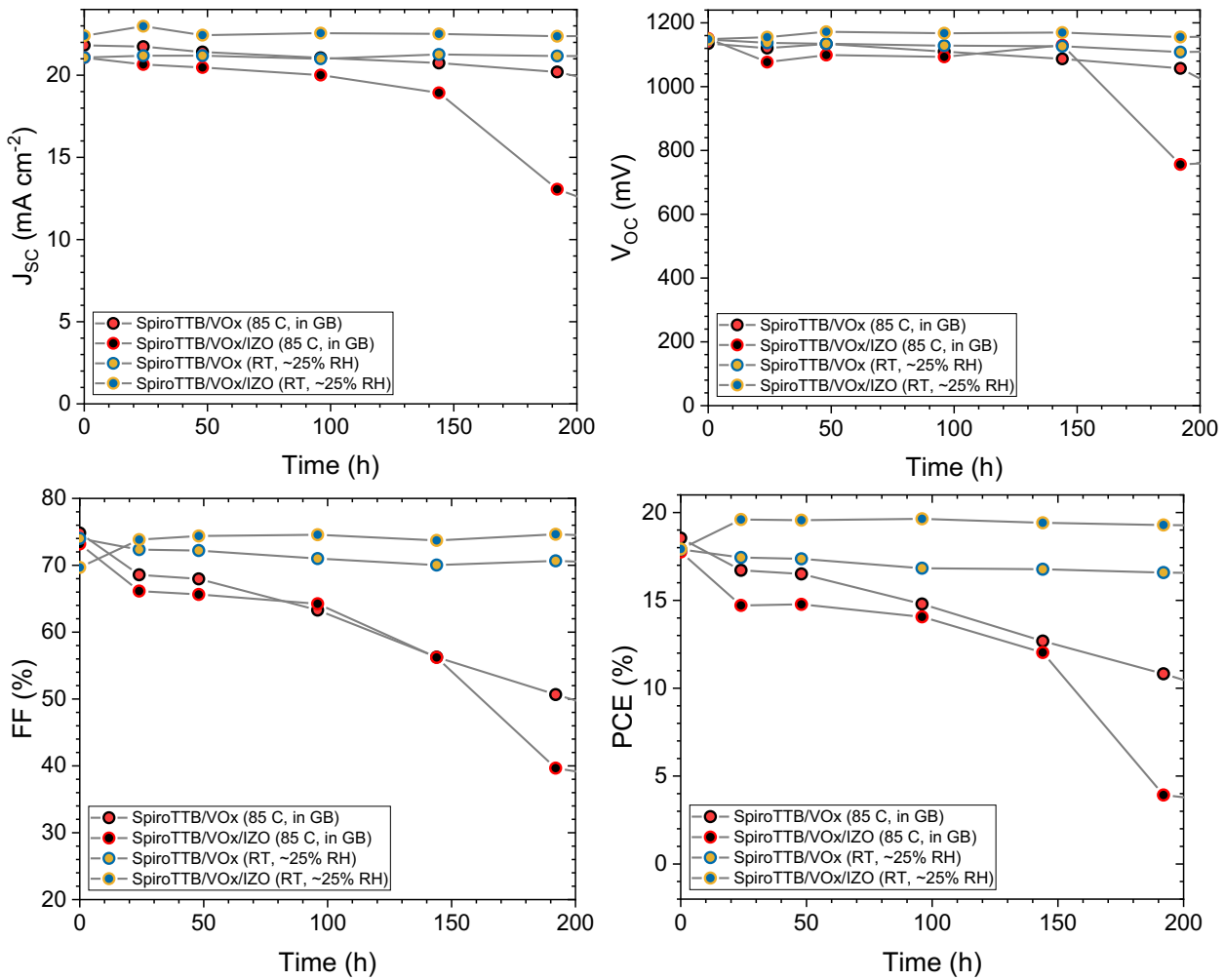


Supplementary Fig. 33. Optical enhancement in tandem solar cell with TCO optimization.

a, EQE curves of the SHJ bottom cells measured from full tandem solar cells with 170 nm rear ITO and IZRO contacts. Here, replacing ITO electrodes by IZRO enables 0.23 mA cm⁻² enhancement on the response of the SHJ bottom cells. Note that here the front TCO is 100 nm IZO, therefore the SHJ bottom cell response is lower than that of the right hand side panel. **b**, EQE curve of the tandems solar cells with 70 and 100 nm front IZO contacts. Here, 70 nm IZO has 60 ohm/sq sheet resistivity while 100 nm has 40 ohm/sq in average.



Supplementary Fig. 34. Encapsulation of the tandem devices for stability tests. **a**, $J-V$ characteristics and **b**, corresponding EQE spectra of the tandem devices before and after encapsulation. Here the chosen device is a random device and does not represent the champion tandems. The J_{sc} losses originate due to the reflection from the front side glass. **c**, The photograph, and **d**, sketch of the glass/glass encapsulated devices. Here, butyl rubber edge sealing is applied between 3 mm low iron glasses. **e**, Temperature profile of the “cell” and the photograph of the devices during the stability measurements. For the encapsulated cells, although the chuck was kept at 25°C , the cell temperature reached $\sim 40^\circ\text{C}$ and stabilized at this value since the devices do not have intimate contact with the back glass, which leads insufficient cooling.



Supplementary Fig. 35. Stability of a- NbO_x based single-junction devices with 1.68 eV perovskites. Here, the ‘85 °C in the GB’ cell represents a condition of keeping the device on the hotplate in a nitrogen glove box to mimic a humidity-free environment but still standard test temperature. In the condition of RT at ~25% RH represents a condition of keeping devices at dark but at room temperature with a constant relative humidity of ~25%. Note that, for the devices without IZO, we used 100 nm gold contacts instead of silver to eliminate the degradation induced by silver.

Supplementary Note 14: Space-charge-limited current (SCLC) and impedance analysis of single-junction opaque devices

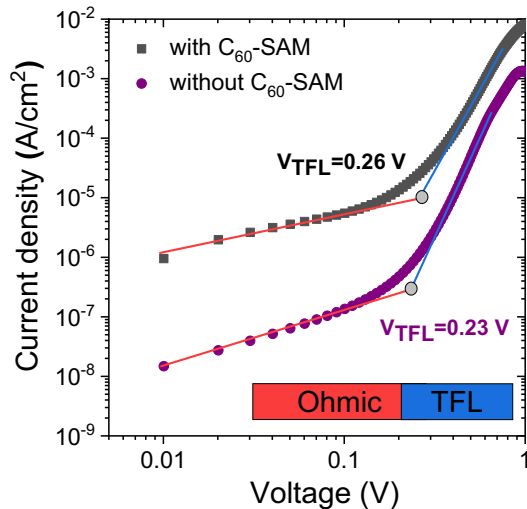
To quantify the electron trap densities, we performed space-charge-limited current (SCLC) measurements on electron only devices with a-NbO_x/Perovskite/PCBM/Ag architecture with and without C₆₀-anchoring.

For this, we recorded current as a function of the applied voltage from the electron only devices, under dark with a Keithley 2400 source meter. Electrical conductivities were extracted from the slope of the linear ohmic regime at low bias. Also, the devices showed the typical nonlinear dark current-voltage plots, where the current is limited by the trap-assisted space charge conduction. Trap densities were calculated by using the following equation;

$$n_{\text{traps}} = 2\epsilon\epsilon_0 V_{\text{TFL}}/qd^2$$

where VTFL is the onset voltage of the trap-filled-limit, q is the electronic charge, d is the thickness of the perovskite, ϵ is the dielectric constant of the material (25.5)⁶⁶ and ϵ_0 is the vacuum permittivity.

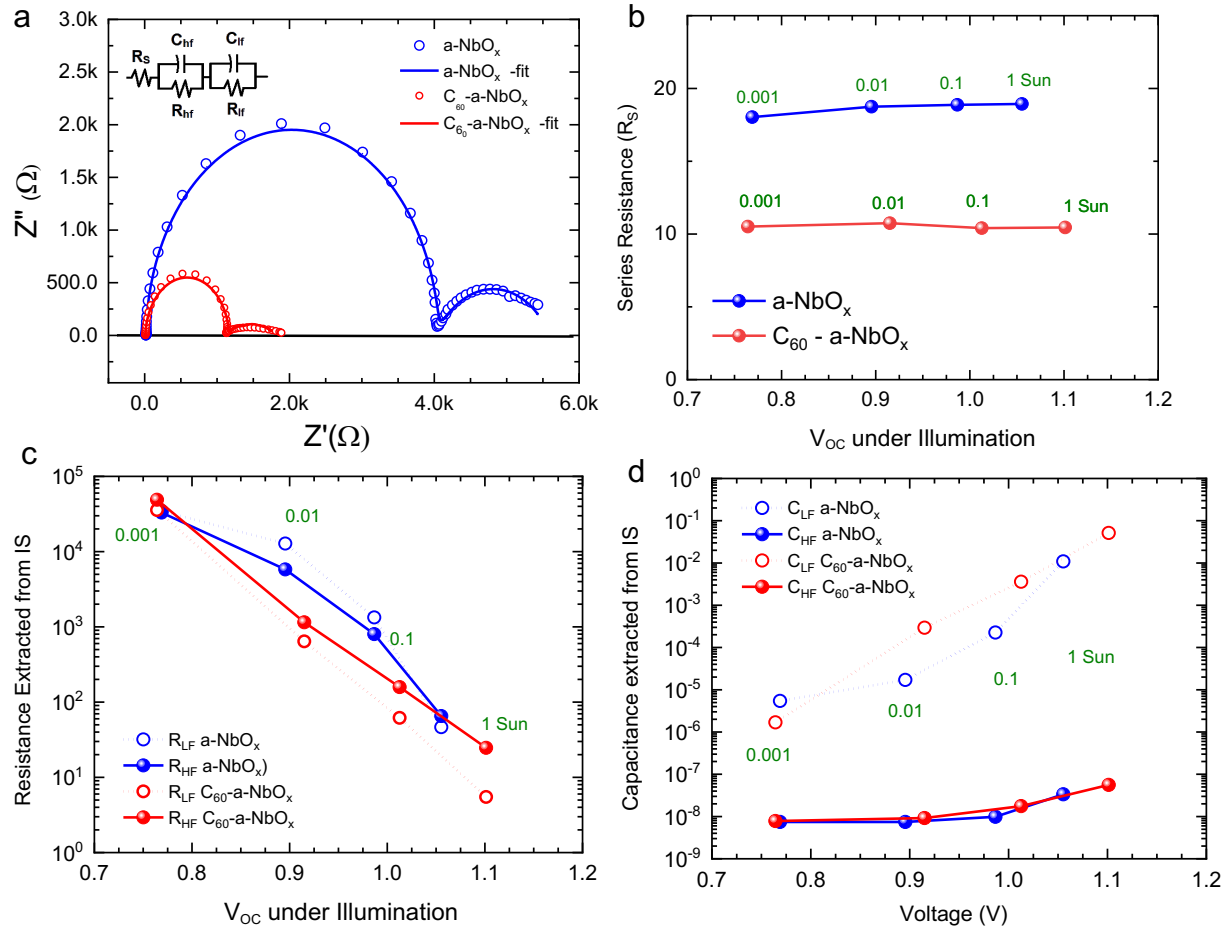
We found that there is no considerable difference in terms of electron trap densities as average trap densities of both conditions is about $1.75 \times 10^{15} \text{ cm}^{-3}$. Such values are considerably lower than the reported literature values with np-SnO_x and TiO₂ ESLs, which are generally in the range of 10^{16} cm^{-3} .^{67,68} This suggests that the a-NbO_x-based devices exhibit low electron trap density within the perovskite layer and at the interfaces. On the other hand, C₆₀-anchoring reduces contact resistivity, which is extracted from the ohmic region of the SCLC graphs.



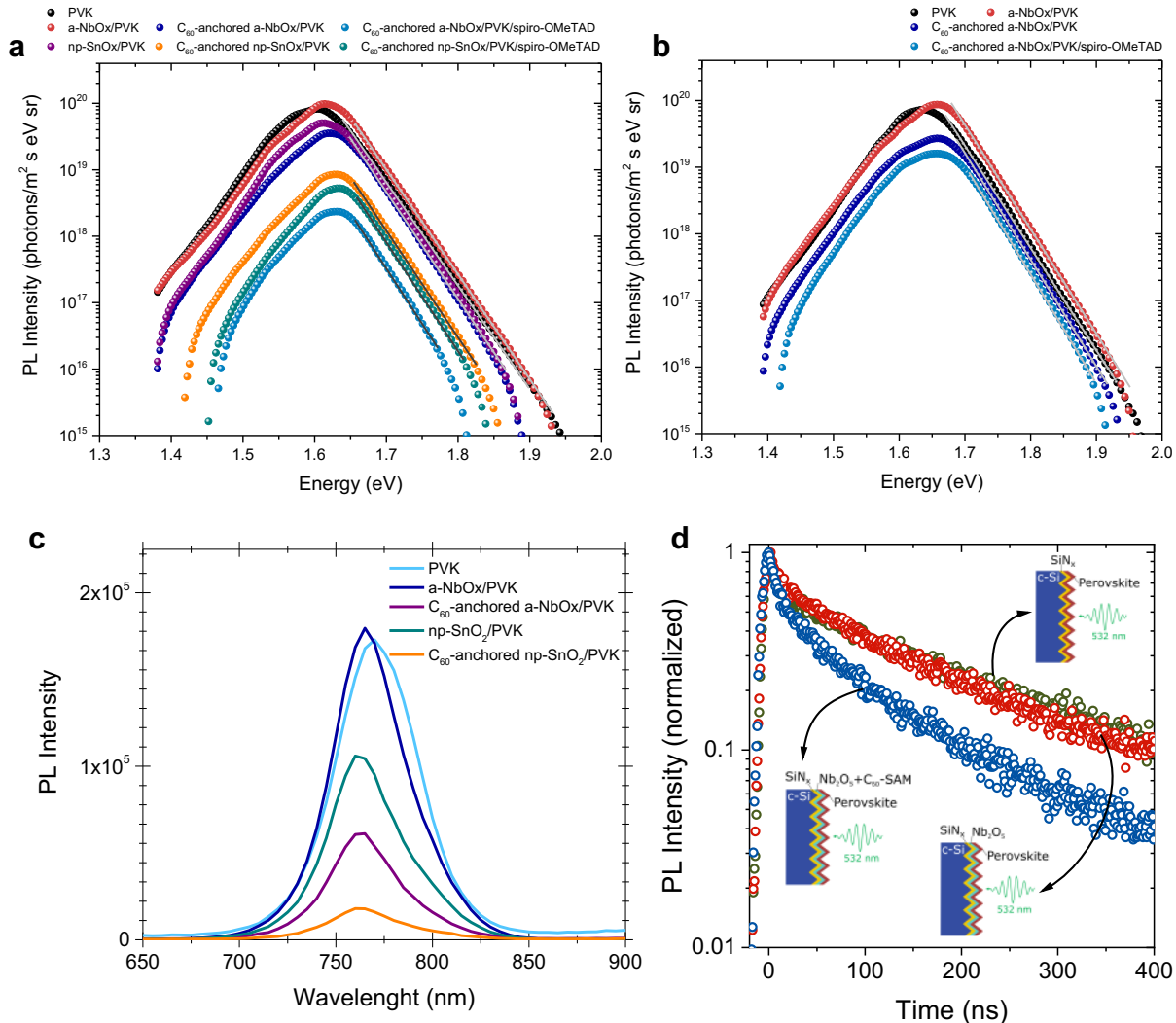
Supplementary Fig. 36. SCLC analysis of single-junction devices based on a-NbO_x ESLs.
SCLC curves of the electron only devices with and without C₆₀-anchoring.

Supplementary Note- 15: Impedance analysis of single-junction opaque devices

Supplementary Figure 37a shows the impedance measurements performed from 10 MHz to 1 mHz at V_{oc} for an illumination light intensity of 0.01 suns and the corresponding fit using equivalent circuit shown in the inset. We performed the impedance measurements at V_{OC} under different illumination intensities and plot the results in Supplementary Figure 37b. This figure shows the corresponding series resistance extracted, indicating a significant reduction in overall series resistance for C_{60} anchored a-NbO_x-based devices.

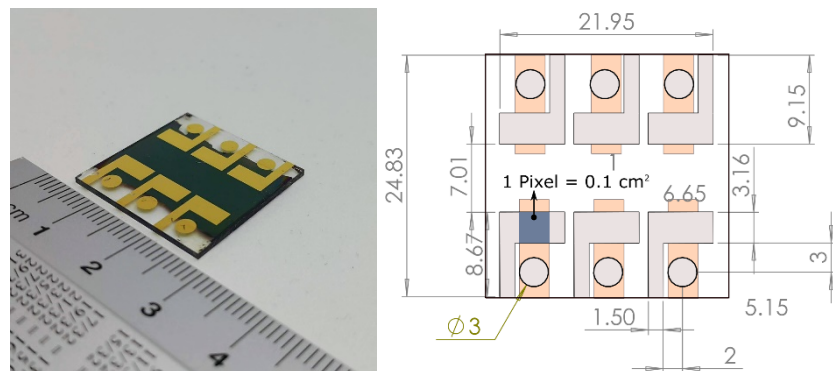


Supplementary Fig. 37. Impedance analysis of the a-NbO_x and C₆₀-anchored a-NbO_x contacts. **a**, Nyquist plot from impedance spectroscopy (IS) measurements and the corresponding fitting for single-junction perovskite devices based on a-NbO_x and C₆₀-anchored a-NbO_x at V_{oc} condition under 0.01-sun illumination. (Inset: Equivalent circuit diagram model used for fitting the IS measurement). **b**, Series resistance extracted from Nyquist plot at V_{OC} for both devices at different illumination intensities. **c**, Low and high resistance extracted from impedance measurements at V_{OC} using various illumination intensities. **d**, The low and high-frequency capacitance values extracted from the IS measurements. Here, we performed measurements on the single-junction devices with, as sketched in Figure 2a.

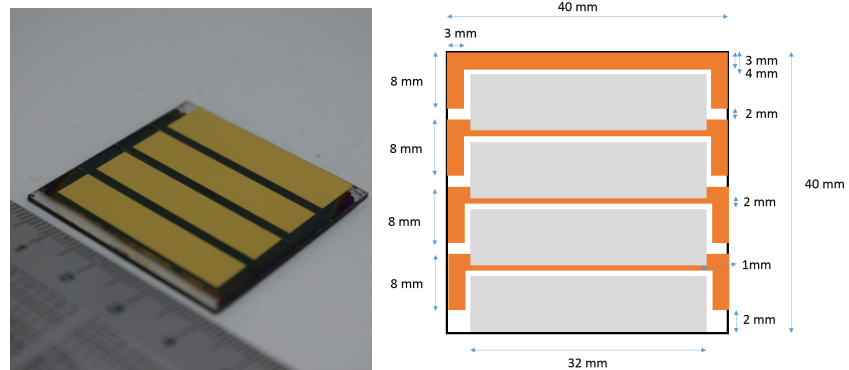


Supplementary Fig. 38. PL analysis of perovskite layers with and without charge selective layers. Absolute PL spectra of perovskite and perovskite/transport layer stacks for **a**, 1.61 eV and **b**, 1.68 eV bandgap perovskites. The high energy tail of the spectra is fitted to get QFLS values of the samples. The measurement was done at 532 nm excitation under 1-sun illumination condition. **c**, steady-state PL spectra and **d**, PL decay of the a-NbO_x/perovskite stacks on textured c-Si/SiN_x substrates without and with C₆₀-SAM layers. Here, in contrast to the quartz/a-NbO_x/perovskite sample, we found that without C₆₀-anchoring between a-NbO_x and perovskite, the PL decay remained unchanged on textured c-Si/SiN_x substrates. The difference is due to the fact that for the quartz substrates, we excited the samples from the ESL side since the effect of interfacial recombination and charge extraction on PL kinetics can be observed more prominently due to the penetration depth of the excitation beam. Thus, for both perovskite and a-NbO_x/perovskite, the surface and bulk defects of the perovskite dominate the PL kinetics instead of the a-NbO_x interface in this condition.

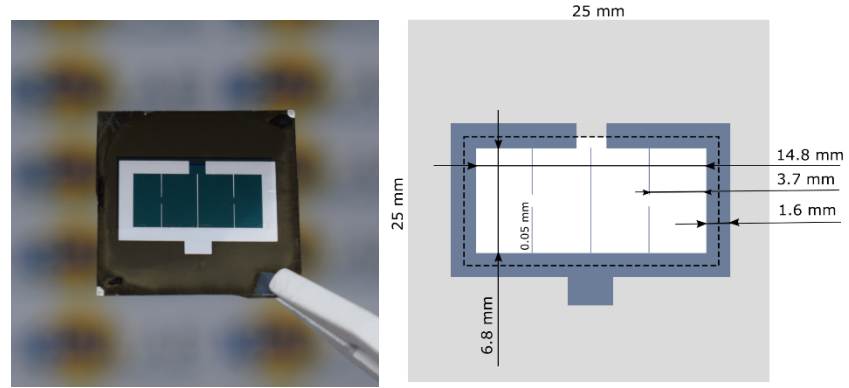
Single junction perovskite solar cells



Perovskite mini-module



Perovskite/silicon tandem solar cells



Supplementary Fig. 39. Device contact layouts. Contact layouts for single-junction perovskite, perovskite mini-module, perovskite/silicon tandem solar cells.

References

1. N. Özer, M. D. Rubin and C. M. Lampert, *Solar Energy Materials and Solar Cells*, 1996, **40**, 285-296.
2. W. Ke, G. Fang, Q. Liu, L. Xiong, P. Qin, H. Tao, J. Wang, H. Lei, B. Li, J. Wan, G. Yang and Y. Yan, *J Am Chem Soc*, 2015, **137**, 6730-6733.
3. R. Lorenz, M. O'Sullivan, A. Fian, D. Sprenger, B. Lang and C. Mitterer, *Thin Solid Films*, 2018, **660**, 335-342.
4. S. Gubbala, H. B. Russell, H. Shah, B. Deb, J. Jasinski, H. Rypkema and M. K. Sunkara, *Energ Environ Sci*, 2009, **2**, 1302-1309.
5. Y.-L. Han, Y.-W. Fang, Z.-Z. Yang, C.-J. Li, L. He, S.-C. Shen, Z.-Z. Luo, G.-L. Qu, C.-M. Xiong, R.-F. Dou, X. Wei, L. Gu, C.-G. Duan and J.-C. Nie, *Physical Review B*, 2015, **92**, 115304.
6. T. Bu, J. Li, F. Zheng, W. Chen, X. Wen, Z. Ku, Y. Peng, J. Zhong, Y.-B. Cheng and F. Huang, *Nature Communications*, 2018, **9**, 4609.
7. K. Akaike, K. Kanai, Y. Ouchi and K. Seki, *Applied Physics Letters*, 2009, **94**, 043309.
8. M. A. Aegeerter, *Solar Energy Materials and Solar Cells*, 2001, **68**, 401-422.
9. A. Foroughi-Abari and K. C. Cadieu, *Thin Solid Films*, 2011, **519**, 3068-3073.
10. R. A. Rani, A. S. Zoolfakar, A. P. O'Mullane, M. W. Austin and K. Kalantar-Zadeh, *Journal of Materials Chemistry A*, 2014, **2**, 15683-15703.
11. T. D. Jun Peng, Xianzhong Zhou, Heping Shen, Yiliang Wu, Hemant Kumar Mulmudi, Yimao Wan, Dingyong Zhong, Juntao Li, Takuya Tsuzuki, Klaus J. Weber, Kylie R. Catchpole, Thomas P. White, *Advanced Energy Materials*, 2016, DOI: 10.1002/aenm.201601768, 1-10.
12. E. M. Miller, Y. Zhao, C. C. Mercado, S. K. Saha, J. M. Luther, K. Zhu, V. Stevanović, C. L. Perkins and J. van de Lagemaat, *Physical Chemistry Chemical Physics*, 2014, **16**, 22122-22130.
13. Y. Guo, J. Tao, F. Shi, X. Hu, Z. Hu, K. Zhang, W. Cheng, S. Zuo, J. Jiang and J. Chu, *ACS Applied Energy Materials*, 2018, **1**, 2000-2006.
14. X. Ling, J. Yuan, D. Liu, Y. Wang, Y. Zhang, S. Chen, H. Wu, F. Jin, F. Wu, G. Shi, X. Tang, J. Zheng, S. Liu, Z. Liu and W. Ma, *ACS Applied Materials & Interfaces*, 2017, **9**, 23181-23188.
15. D. Shen, W. Zhang, Y. Li, A. Abate and M. Wei, *ACS Applied Nano Materials*, 2018, DOI: 10.1021/acsanm.8b00859.
16. Z. Wang, J. Lou, X. Zheng, W.-H. Zhang and Y. Qin, *ACS Sustainable Chemistry & Engineering*, 2019, DOI: 10.1021/acssuschemeng.9b00991.
17. *Nano Energy*, 2017, DOI: 10.1016/j.nanoen.2017.04.010.
18. B. Gu, Y. Zhu, H. Lu, W. Tian and L. Li, *Solar Energy*, 2018, **166**, 187-194.
19. Y. Guo, J. Tao, J. Jiang, J. Zhang, J. Yang, S. Chen and J. Chu, *Solar Energy Materials and Solar Cells*, 2018, **188**, 66-72.
20. M. Kam, Q. Zhang, D. Zhang and Z. Fan, *Scientific Reports*, 2019, **9**, 6963.
21. L. Qiu, Z. Liu, L. K. Ono, Y. Jiang, D.-Y. Son, Z. Hawash, S. He and Y. Qi, *Advanced Functional Materials*, **0**, 1806779.
22. L. Kegelmann, C. M. Wolff, C. A. Omondi, F. Lang, E. L. Unger, L. Korte, T. Dittrich, D. Neher, B. Rech and S. Albrecht, *ACS Applied Materials & Interfaces*, 2017, DOI: 10.1021/acsmami.7b00900.

23. K.-H. Jung, J.-Y. Seo, S. Lee, H. Shin and N.-G. Park, *Journal of Materials Chemistry A*, 2017, DOI: 10.1039/C7TA08040A.
24. Y. Kuang, V. Zardetto, R. van Gils, S. Karwal, D. Koushik, M. A. Verheijen, L. E. Black, C. Weijtens, S. Veenstra, R. Andriessen, W. M. M. Kessels and M. Creatore, *ACS Applied Materials & Interfaces*, 2018, DOI: 10.1021/acsami.8b09515.
25. Q. Jiang, L. Zhang, H. Wang, X. Yang, J. Meng, H. Liu, Z. Yin, J. Wu, X. Zhang and J. You, *Nature Energy*, 2016, DOI: doi:10.1038/nenergy.2016.177.
26. T. Minemoto and M. Murata, *Solar Energy Materials and Solar Cells*, 2015, **133**, 8-14.
27. P. Caprioglio, M. Stolterfoht, C. M. Wolff, T. Unold, B. Rech, S. Albrecht and D. Neher, *Advanced Energy Materials*, 2019, **9**, 1901631.
28. H. J. Snaith and M. Grätzel, *Advanced Materials*, 2007, **19**, 3643-3647.
29. Y. Raoui, H. Ez-Zahraouy, S. Kazim and S. Ahmad, *Journal of Energy Chemistry*, 2021, **54**, 822-829.
30. T. P. I. Saragi, T. Fuhrmann-Lieker and J. Salbeck, *Advanced Functional Materials*, 2006, **16**, 966-974.
31. S. D. Stranks, G. E. Eperon, G. Grancini, C. Menelaou, M. J. P. Alcocer, T. Leijtens, L. M. Herz, A. Petrozza and H. J. Snaith, *Science*, 2013, **342**, 341-344.
32. T. Hwang, A. J. Yun, J. Kim, D. Cho, S. Kim, S. Hong and B. Park, *ACS Applied Materials & Interfaces*, 2019, **11**, 6907-6917.
33. V. V. Brus, A. K. K. Kyaw, P. D. Maryanchuk and J. Zhang, *Progress in Photovoltaics: Research and Applications*, 2015, **23**, 1526-1535.
34. B. Macco, M. Bivour, J. H. Deijkers, S. B. Basuvalingam, L. E. Black, J. Melskens, B. W. H. v. d. Loo, W. J. H. Berghuis, M. Hermle and W. M. M. Kessels, *Applied Physics Letters*, 2018, **112**, 242105.
35. B. Liao, B. Hoex, A. G. Aberle, D. Chi and C. S. Bhatia, *Applied Physics Letters*, 2014, **104**, 253903.
36. F. Werner and J. Schmidt, *Applied Physics Letters*, 2014, **104**, 091604.
37. J. H. R. Enslin and D. B. Snyman, 1992.
38. H. Ying-Tung and C. China-Hong, 2002.
39. M. De Bastiani, G. Dell'Erba, M. Gandini, V. D'Innocenzo, S. Neutzner, A. R. S. Kandada, G. Grancini, M. Binda, M. Prato, J. M. Ball, M. Caironi and A. Petrozza, *Advanced Energy Materials*, 2016, **6**, 1501453.
40. M. De Bastiani, E. Aydin, T. Allen, D. Walter, A. Fell, J. Peng, N. Gasparini, J. Troughton, D. Baran, K. Weber, T. P. White and S. De Wolf, *Advanced Electronic Materials*, 2018, **0**, 1800500.
41. P. Liu, W. Wang, S. Liu, H. Yang and Z. Shao, *Advanced Energy Materials*, 2019, **9**, 1803017.
42. Y. Rong, Y. Hu, S. Ravishankar, H. Liu, X. Hou, Y. Sheng, A. Mei, Q. Wang, D. Li, M. Xu, J. Bisquert and H. Han, *Energ Environ Sci*, 2017, DOI: 10.1039/C7EE02048A.
43. G. A. Nemnes, C. Besleaga, V. Stancu, D. E. Dogaru, L. N. Leonat, L. Pintilie, K. Torfason, M. Ilkov, A. Manolescu and I. Pintilie, *The Journal of Physical Chemistry C*, 2017, **121**, 11207-11214.
44. Y. Hou, E. Aydin, M. De Bastiani, C. Xiao, F. H. Isikgor, D.-J. Xue, B. Chen, H. Chen, B. Bahrami, A. H. Chowdhury, A. Johnston, S.-W. Baek, Z. Huang, M. Wei, Y. Dong, J. Troughton, R. Jalmoode, A. J. Mirabelli, T. G. Allen, E. Van Kerschaver, M. I.

- Saidaminov, D. Baran, Q. Qiao, K. Zhu, S. De Wolf and E. H. Sargent, *Science*, 2020, **367**, 1135-1140.
45. B. Chen, S.-W. Baek, Y. Hou, E. Aydin, M. De Bastiani, B. Scheffel, A. Proppe, Z. Huang, M. Wei, Y.-K. Wang, E.-H. Jung, T. G. Allen, E. Van Kerschaver, F. P. García de Arquer, M. I. Saidaminov, S. Hoogland, S. De Wolf and E. H. Sargent, *Nature Communications*, 2020, **11**, 1257.
46. E. Aydin, J. Troughton, M. De Bastiani, E. Ugur, M. Sajjad, A. Alzahrani, M. Neophytou, U. Schwingenschlögl, F. Laquai, D. Baran and S. De Wolf, *ACS Applied Energy Materials*, 2018, DOI: 10.1021/acsaem.8b01263.
47. J. Xu, C. C. Boyd, Z. J. Yu, A. F. Palmstrom, D. J. Witter, B. W. Larson, R. M. France, J. Werner, S. P. Harvey, E. J. Wolf, W. Weigand, S. Manzoor, M. F. A. M. van Hest, J. J. Berry, J. M. Luther, Z. C. Holman and M. D. McGehee, *Science*, 2020, **367**, 1097-1104.
48. Y. Lee, S. Lee, G. Seo, S. Paek, K. T. Cho, A. J. Huckaba, M. Calizzi, D.-w. Choi, J.-S. Park, D. Lee, H. J. Lee, A. M. Asiri and M. K. Nazeeruddin, *Advanced Science*, 2018, **5**, 1800130.
49. J. Werner, L. Barraud, A. Walter, M. Bräuninger, F. Sahli, D. Sacchetto, N. Tétreault, B. Paviet-Salomon, S.-J. Moon, C. Allebé, M. Despeisse, S. Nicolay, S. D. Wolf, B. Niesen and C. Ballif, *ACS Energy Letters*, 2016, **1**, 474–480.
50. S. Albrecht, M. Saliba, J. P. Correa Baena, F. Lang, L. Kegelmann, M. Mews, L. Steier, A. Abate, J. Rappich, L. Korte, R. Schlatmann, M. K. Nazeeruddin, A. Hagfeldt, M. Grätzel and B. Rech, *Energ Environ Sci*, 2016, **9**, 81-88.
51. J. Werner, C. H. Weng, A. Walter, L. Fesquet, J. P. Seif, S. De Wolf, B. Niesen and C. Ballif, *J Phys Chem Lett*, 2016, **7**, 161-166.
52. F. Sahli, B. A. Kamino, J. Werner, M. Bräuninger, B. Paviet-Salomon, L. Barraud, R. Monnard, J. P. Seif, A. Tomasi, Q. Jeangros, A. Hessler-Wyser, S. De Wolf, M. Despeisse, S. Nicolay, B. Niesen and C. Ballif, *Advanced Energy Materials*, 2017, DOI: 10.1002/aenm.201701609, 1701609-n/a.
53. F. Hou, L. Yan, B. Shi, J. Chen, S. Zhu, Q. Ren, S. An, Z. Zhou, H. Ren, C. Wei, Q. Huang, G. Hou, X. Chen, Y. Li, Y. Ding, G. Wang, D. Zhang, Y. Zhao and X. Zhang, *ACS Applied Energy Materials*, 2019, DOI: 10.1021/acsaem.8b00926.
54. J. Zheng, C. F. J. Lau, H. Mehrvarz, F.-J. Ma, Y. Jiang, X. Deng, A. Soeriyadi, J. Kim, M. Zhang, L. Hu, X. Cui, D. S. Lee, J. Bing, Y. Cho, C. Chen, M. A. Green, S. Huang and A. W. Y. Ho-Baillie, *Energy & Environmental Science*, 2018, **11**, 2432-2443.
55. J. Zheng, H. Mehrvarz, C. Liao, J. Bing, X. Cui, Y. Li, V. R. Gonçales, C. F. J. Lau, D. S. Lee, Y. Li, M. Zhang, J. Kim, Y. Cho, L. G. Caro, S. Tang, C. Chen, S. Huang and A. W. Y. Ho-Baillie, *ACS Energy Letters*, 2019, **4**, 2623-2631.
56. J. Zheng, H. Mehrvarz, F.-J. Ma, C. F. J. Lau, M. A. Green, S. Huang and A. W. Y. Ho-Baillie, *ACS Energy Letters*, 2018, DOI: 10.1021/acsenergylett.8b01382, 2299-2300.
57. H. Shen, S. T. Omelchenko, D. A. Jacobs, S. Yalamanchili, Y. Wan, D. Yan, P. Phang, T. Duong, Y. Wu, Y. Yin, C. Samundsett, J. Peng, N. Wu, T. P. White, G. G. Andersson, N. S. Lewis and K. R. Catchpole, *Science Advances*, 2018, **4**, eaau9711.
58. E. Aydin, T. G. Allen, M. De Bastiani, L. Xu, J. Ávila, M. Salvador, E. Van Kerschaver and S. De Wolf, *Nature Energy*, 2020, DOI: 10.1038/s41560-020-00687-4.
59. D. Kim, H. J. Jung, I. J. Park, B. W. Larson, S. P. Dunfield, C. Xiao, J. Kim, J. Tong, P. Boonmongkolras, S. G. Ji, F. Zhang, S. R. Pae, M. Kim, S. B. Kang, V. Dravid, J. J.

- Berry, J. Y. Kim, K. Zhu, D. H. Kim and B. Shin, *Science*, 2020, DOI: 10.1126/science.aba3433, eaba3433.
60. B. Chen, Z. J. Yu, S. Manzoor, S. Wang, W. Weigand, Z. Yu, G. Yang, Z. Ni, X. Dai, Z. C. Holman and J. Huang, *Joule*, 2016, DOI: 10.1016/j.joule.2020.01.008.
61. A. Al-Ashouri, E. Köhnen, B. Li, A. Magomedov, H. Hempel, P. Caprioglio, J. A. Márquez, A. B. Morales Vilches, E. Kasparavicius, J. A. Smith, N. Phung, D. Menzel, M. Grischek, L. Kegelmann, D. Skroblin, C. Gollwitzer, T. Malinauskas, M. Jošt, G. Matič, B. Rech, R. Schlatmann, M. Topič, L. Korte, A. Abate, B. Stannowski, D. Neher, M. Stolterfoht, T. Unold, V. Getautis and S. Albrecht, *Science*, 2020, **370**, 1300-1309.
62. J. Werner, G. Dubuis, A. Walter, P. Löper, S.-J. Moon, S. Nicolay, M. Morales-Masis, S. De Wolf, B. Niesen and C. Ballif, *Solar Energy Materials and Solar Cells*, 2015, **141**, 407-413.
63. J. Werner, J. Geissbuhler, A. Dabirian, S. Nicolay, M. Morales-Masis, S. D. Wolf, B. Niesen and C. Ballif, *ACS Appl Mater Interfaces*, 2016, **8**, 17260-17267.
64. J. A. Raiford, R. A. Belisle, K. A. Bush, R. Prasanna, A. F. Palmstrom, M. D. McGehee and S. Bent, *Sustainable Energy & Fuels*, 2019, DOI: 10.1039/C9SE00081J.
65. J. Meyer, S. Hamwi, M. Kröger, W. Kowalsky, T. Riedl and A. Kahn, *Advanced Materials*, 2012, **24**, 5408-5427.
66. D. Shi, V. Adinolfi, R. Comin, M. Yuan, E. Alarousu, A. Buin, Y. Chen, S. Hoogland, A. Rothenberger, K. Katsiev, Y. Losovyj, X. Zhang, P. A. Dowben, O. F. Mohammed, E. H. Sargent and O. M. Bakr, *Science*, 2015, **347**, 519-522.
67. D. Yang, R. Yang, K. Wang, C. Wu, X. Zhu, J. Feng, X. Ren, G. Fang, S. Priya and S. Liu, *Nature Communications*, 2018, **9**, 3239.
68. F. Cai, L. Yang, Y. Yan, J. Zhang, F. Qin, D. Liu, Y.-B. Cheng, Y. Zhou and T. Wang, *Journal of Materials Chemistry A*, 2017, **5**, 9402-9411.